March 3, 2023

A role for retro-splenial cortex in the task-related P3 network

Diptyajit Das[1], Marnie E. Shaw[2], Matti S. Hämäläinen[3,4,5], Andrew R. Dykstra[6], Laura Doll[1], and Alexander Gutschalk[1,*]

[1] Department of Neurology, Ruprecht-Karls-Universität Heidelberg, Im Neuenheimer Feld 400, 69120 Heidelberg, Germany

[2] College of Engineering & Computer Science, Australian National University, Canberra, Australia

[3] Athinoula A. Martinos Center for Biomedical Imaging, Massachusetts General Hospital, USA

[4] Harvard, MIT Division of Health Science and Technology, USA

[5] Department of Neuroscience and Biomedical Engineering, Aalto University school of Science, Finland

[6] Department of Biomedical Engineering, University of Miami, Coral Gables, USA

*Corresponding author: Alexander.Gutschalk@med.uni-heidelberg.de

Abstract

The P3 is an event-related response observed in relation to task-relevant sensory events. Despite its ubiquitous presence, the generators of the P3 are controversial and not well identified. Here, we compared source analysis of combined magneto- and electro–encephalography (MEG and EEG) data with fMRI and simulation studies to better understand the sources of the P3 in an auditory oddball paradigm. Our results suggest that the dominant source of the classical, postero-central P3 lies in the retro-splenial cortex of the ventral cingulate gyrus. A second P3 source in the anterior insular cortex contributes little to the postero-central maximum. Multiple other sources in the auditory, somatosensory, and anterior middle cingulate cortex are active in an overlapping time window but can be functionally dissociated based on their activation time courses. These results provide a new perspective for the interpretation of the extensive research based on the P3 response.

Keywords: P300, retro-splenial cortex, insular cortex, EEG, MEG, fMRI, source analysis

Introduction

Many tasks that we perform in response to sensory events recruit widespread cortical networks [Hugdahl et al., 2015; Kim, 2014] as detected by functional magnetic resonance imaging (fMRI). In electroencephalography (EEG), such task-relevant stimuli ubiquitously evoke the prominent P3 [Sutton et al., 1965], also called P300, which has been explored by a large number of cognitive neuroscience studies including such diverse fields as consciousness [Sergent et al., 2005], mental disorders [Hamilton et al., 2020], or brain-computer interfaces [Chaudhary et al., 2016]. Two variants of the P3 have been studied: the earlier P3a is evoked by rare, salient events which are not assigned as target in an active task; it is recorded over more anterior sites in EEG. The later P3b is only observed for task-relevant target events with an amplitude maximum over more posterior sites [Hillyard et al., 1971; Squires et al., 1975]. There are numerous models of the potential psychological processes related to the P3, a summary of which is beyond the scope of this paper [Polich, 2007; Verleger, 2020]. The focus of the present study is on the P3b, but the paradigm used will be expected to evoke some P3a as well, which is why we will refer to the response below simply as P3.

Defining the functional role of the P3 in a neuroanatomically constrained model has been limited by ambiguous findings concerning its neural generators: Early intracranial EEG (iEEG) recordings in patients with epilepsy demonstrated P3-like responses in the hippocampus [Halgren et al., 1980], but subsequent studies in patients with lesions of middle temporal lobe structures demonstrated that the hippocampus is not the source of the P3 as measured by scalp EEG [Johnson, 1988; Onofrj et al., 1992]. Further iEEG studies showed that P3-like responses can be observed by electrodes in many other brain areas [Halgren et al., 1995b; Halgren et al., 1995a], and it was suggested that the neural generator of the P3 is distributed across multiple brain areas, including temporal, frontal, and parietal lobes, as well as the cingulate gyrus. This view was further supported by fMRI, which has been used to constrain source models of the P3 recorded in EEG [Bledowski et al., 2004; Li et al., 2020; Linden et al., 1999; Mulert et al., 2004a; Mulert et al., 2004b]. In

agreement with other fMRI studies [Kim, 2014], these constrained source models suggested potential generators of the P3 in the pre-central sulcus (PCS), intra-parietal sulcus (IPS), supplementary motor area (SMA), midcingulate cortex (MCC), insular cortex, and temporo-parietal junction (TPJ). A potential role of the TPJ has been independently emphasized by studies in patients with structural brain lesions [Knight et al., 1989; Verleger et al., 1994; Yamaguchi and Knight, 1991]. Source analysis of the P3 in magnetoencephalography (MEG) has typically suggested sources in the deep [Rogers et al., 1993; Tarkka et al., 1995] temporal lobes, but others reported that the P3 was not obtained reliably at all in MEG [Siedenberg et al., 1996]. Currently, it is widely held that the P3 is generated by the same areas observed active during target detection of rare events in fMRI [Bledowski et al., 2004; Kim, 2014; Mulert et al., 2004b], i.e., in TPJ, dorsal frontal and parietal cortex, and in the MCC and SMA. In other contexts, however, fMRI has been suggested to be linked with gamma activity rather than with evoked potentials in lower frequency bands [Niessing et al., 2005; Steinmann and Gutschalk, 2011], and a detailed investigation of how activity in defined anatomical areas would generate the spatial distribution of the P3 observed in EEG and MEG is still lacking.

The present study assessed the neural generators of the P3 by employing combined M/EEG recordings and source analysis in a classical auditory oddball paradigm [Ritter et al., 1972], and directly compared such source analysis results to fMRI. Our results suggest a different source configuration for the P3 than summarized above, with one source lying in retro-splenial cortex (RSC), and another source lying in insular cortex. This P3 activity is paralleled by activity in multiple other areas, including auditory cortex (AC), left primary somato-sensory cortex (S1), and anterior MCC (aMCC), which can be dissociated from the P3 by their activation time courses. In the second part of the paper, we simulated the scalp EEG and sensor MEG distribution based on circumscribed sources in these regions to evaluate (i) their contribution to the centro-parietal P3 that is typically evaluated in EEG, and (ii) to control for the interaction between remote source areas. Finally, we tested which of the simulated sources can explain the data at the P3 peak. Results suggest that the source in RSC explains more variance of the data than other sources.

Materials and Methods

Participants

A total of fifteen healthy young adults (female, 8; male 7) with a mean age of 26.8 years (range 20 - 45) with no previous history of neurological or hearing disorder participated in this study. This sample size was based on experience from previous studies using similar source analysis techniques. The data of three participants were excluded later from the analysis due to large measurement artifacts (n=2) and incomplete recording (n=1). The study was approved by the ethics committee of Heidelberg University, Germany and each volunteer provided written informed consent before participation.

Experimental design and procedure

Simultaneous M/EEG data were recorded while presenting a classical auditory oddball sequence consisting of frequent standard (1000 Hz) and rare (14%) deviant (900 Hz) tones. fMRI data were recorded using the same stimuli within a separate session. Tones of 75 ms duration were presented with an average 2-s inter-stimulus interval, randomly jittered by ± 0.5s. A total of 1274 tones were presented across 3 separate runs. Listeners were instructed to press a button with their right index finger to identify all deviant tones. For both M/EEG and fMRI measurements, participants were presented with the same stimuli, with a short break in between the three runs. In MEG, stimuli were presented diotically with ER-3 earphones (Etymotics Research, Elk Grove Village, IL, USA) via foam earpieces. In fMRI, stimuli were presented diotically via MR-compatible S14 insert earphones (Sensimetrics Corporation, Gloucester, MA, USA), which attenuate the scanner noise by approximately 15-20dB. Sound level was individually adjusted to be at a comfortable listening level. All sound stimuli were generated using PsychoPy software (www.psychopy.org) [Peirce, 2007].

Data acquisition

MEG data were acquired at a sampling rate of 1000 Hz (using a 330 Hz online low-pass filter) inside a four-layer magnetically shielded room (IMEDCO) via a Neuromag-122 whole-head system

109 (MEGIN OY, Helsinki, Finland) equipped with 61 dual-channel planar first-order gradiometers.
110 Participants' head geometry and location of four head-position indicator coils were digitized
111 together with the EEG electrode positions relative to a coordinate system spanned by the nasion
112 and two pre-auricular points using a Polhemus Isotrack II digitizer (Colchester, VT, USA). EEG data
113 were recorded using an Easycap (Herrsching, Germany) M64 recording cap with a 64-channel
114 10%-system montage. The EEG was amplified with two 32-channel Neuroscan amplifiers,
115 referenced to Pz, and digitized together with the MEG.

116 MRI data were acquired with a 3T Siemens Magnetom Trio scanner (Siemens Medical Systems,
117 Erlangen, Germany) with a 32-channel coil; fMRI data were acquired with an interleaved echo
118 planar imaging (EPI) sequence (TR=2 sec, TE=30 ms, flip angle 80°) with 32 axial slices aligned
119 along the anterior-posterior commissure line (3.99-mm slices, 3×3 mm^2 in-plane resolution).
120 Structural MRI images with the same field of view were obtained, including T1-weighted anatomical
121 images (GR/MPRAGE, flip angle 9, echo time 2.63, repetition time 1570, resolution 1×1×1 mm^3)
122 and multi-echo fast low-angle shot (FLASH) sequences. These images were used for co-
123 registration with subject-specific M/EEG and fMRI results to standard space and for creating
124 realistic-shaped boundary-element head models. The three scanning runs lasted 800 seconds
125 each and there was a brief break after each run to restart the stimulation and communicate with
126 the participant.

127 **M/EEG data Preprocessing**

128 Preprocessing of M/EEG data was performed using MNE software packages
129 (http://martinos.org/mne) [Gramfort et al., 2013]. For each recording (three runs per participant),
130 first, a visual inspection of the raw M/EEG data was carried out to identify and mark time epochs
131 as well as the channels containing large artifacts or flat signals. A separate denoising was then
132 performed only for the MEG data to reduce uncorrelated sensor noise and artifacts (i.e., flux jumps)
133 using oversampled temporal projection (OTP) [Larson and Taulu, 2018]. This technique allows
134 suppression of sensor-space noise that is spatially uncorrelated with the data. After applying a
135 bandpass filter (0.5-30 Hz) on the M/EEG data, re-referencing of the EEG was performed to an

average reference. Eye blinks and cardiac artifacts were then removed from the data using MNE's independent component analysis algorithm [Hyvärinen, 1999]. Afterwards, the data were epoched from -100 to 1000 ms relative to stimulus onset, yielding two stimulus locked conditions: standard and deviant. A separate epoching window spanning -500 to 500 ms relative to the button press was created to track response-locked brain activity. Thus, three overall data conditions were constructed: standard, deviant, and response-locked. Next, the bad segments of epochs (trials) were repaired using an automatic data driven autoreject [Jas et al., 2017] algorithm implemented in MNE. All remaining deviant and response-locked conditions were included in the average response. The number of averaged standards was reduced to the number of deviants using the 'mintime' function in MNE, to equalize the number of deviant and standard trials for the source analysis.

The source space and gain matrix

To define an individual, cortically constrained source space, FreeSurfer [Dale et al., 1999; Fischl, 2012] was first used to reconstruct the cortical surface (white and pial) from the high-resolution T1-weighted scan (3D MPRAGE data) for each participant. Afterwards, at least 10242 dipoles (i.e., source locations per hemisphere) were placed at the gray-white matter interface to create the source space, with ~3 mm spacing. The individual forward solution was restricted to a cortical source space parcellation, which excludes corpus callosum and areas below that were removed from the source space. The resulting dipole locations correspond to a cortical surface area of about 10 mm^2 on average. High resolution inner-skull, outer-skull, and scalp surfaces created from FLASH images were used to model the electrical conductivity between each surface using a three-compartment boundary-element model (BEM) using MNE. For BEM, 5120 triangles were used for creating the triangulated meshes with respective conductivities of the brain, skull, and skin were assumed to be 0.3 S/m, 0.06 S/m and 0.3 S/m. To define the locations of the EEG electrodes on the scalp and the configuration of the MEG sensors relative to the cortical surface, MNE-coordinate-system alignment tools [Gramfort et al., 2013] were used, where fiducial landmarks (two pre-auricular points and the nasion) are manually identified from the MRI-based rendering of the head

surface [Besl and McKay, 1992]. The tool calculates a transformation by minimizing the digitized scalp surface points with respect to the MRI-defined scalp.

Inverse modeling and source analysis of M/EEG data

The field distribution y(t) of sensor/electrode space M/EEG data can be modeled as a linear combination of the source time courses x(t*)* and noise n(t):

$$y(t) = Gx(t) + n(t) \qquad (1)$$

where, G is the forward gain matrix. To estimate the source current density on the cortical surface for each participant, a separate forward solution for each experimental segment was computed in MNE separately and averaged together [Gramfort et al., 2013; Hämäläinen and Sarvas, 1989; Uutela et al., 2001] for more accurate source estimation. The inverse estimation of active sources (x) is then performed by applying an inverse operator (G´) to the data by using the linear L2 minimum-norm estimator (MNE) such that:

$$x' = G'_{MNE}\, y = G^T(GG^T + \lambda^2 C)^{-1}\, y \qquad (2)$$

where, x´ is an estimation of the true sources x, C is the noise covariance matrix at the sensor/electrode space, and λ is the Tikhonov regularization parameter. In addition to that, a loose orientation constraint of 0.2 was added to the model so that it can remain flexible against co-registration errors [Lin et al., 2006a] Afterwards, the source estimates were normalized to yield a dSPM [Dale et al., 2000]. This step was performed for each condition (i.e., standard, deviant, deviant - standard, and button response) separately. The noise-covariance matrix was calculated from pre-stimulus baseline i.e., 100 ms preceding the stimuli by using an automated advanced regularization method called shrinkage technique [Engemann and Gramfort, 2015]. Subsequently, noise-normalized source-space data from each participant were transformed onto a template brain atlas i.e., the FreeSurfer average brain (fsaverage) using a spherical registration method [Fischl et al., 1999]. This registration was used to accurately align the dSPM results across individuals. The resulting maps across participants were then averaged per evoked condition to create a single grand-average dSPM solution. For the ROI-based analysis, hand-drawn ROIs were defined on the

FreeSurfer average brain based on the anatomy and were then transformed to the individual brain anatomy; ROIs were placed on one side of a sulcus and not across sulci, such that most dipoles within the ROI are expected to have similar dipole orientation and thus polarity. Time-courses per condition were then calculated as average across all dipoles within each ROI, separately for each individual participant. Note that defining a one-polarity ROI for Heschl's gyrus can be complex, because there is often a polarity reversal towards Heschl's sulcus (between Heschl's gyrus and planum temporale). We therefore also explored separate ROIs for the anterior and posterior half of Heschl's gyrus. Because these ROIs revealed similar results for the data of this study, we restricted our analysis to a single ROI defined for the middle of Heschl's gyrus, avoiding the posterior border towards Heschl's sulcus and the anterior border towards the circular sulcus.

Spread analysis of M/EEG data

The point-spread function (PSF) and cross-talk function (CTF) [Hauk et al., 2011] were computed in order to characterize the leakage of current estimates between different ROIs. First, the dSPM-based resolution matrix was computed by multiplying the inverse operator to the forward gain matrix for each ROI. Afterwards, each ROI based PSF and CTF was extracted as the column and the row of that resolution matrix, respectively. This step was then repeated for all individual data set before averaging across participants. Finally, leakage of current estimates and the potential influence of one ROI to another were calculated as the absolute correlation between ROIs for PSFs and CTFs.

Statistical tests and reproducibility

The statistical difference among ROI-based source-level time courses between standards and deviants was assessed through a two-sample cluster-based permutation test [Maris and Oostenveld, 2007] across participants. The statistical test is a non-parametric test that is designed to solve the multiple comparisons problem (MCP) during hypothesis testing. In detail, first, an F statistic is computed at each participant-specific ROI-based source-space data sample (every 2 ms from -100ms to 1000ms relative to stimulus onset) from each data condition. A cluster threshold (p

215 < 0.01) drawn from a standard F distribution was then applied at each sample, keeping only the
216 statistically significant samples to form clusters whose values were higher than the applied
217 threshold. Afterwards, the cluster-level statistic is defined within each cluster by taking the sum of
218 its absolute test statistics. Then, a maximum cluster-level permutation distribution was constructed
219 by using the cluster statistics computed under a Monte Carlo estimation [Ernst, 2004] with random
220 shuffling and 100001 iterations. Cluster level p-values were estimated by computing the proportion
221 that resulted in some larger cluster-level statistics than the actual one calculated from the maximum
222 cluster-level permutation distribution. Significant cluster p-values were defined by correcting the p-
223 values using a Bonferroni correction i.e., critical alpha level ($\alpha = 0.05$) was set to ($\alpha^* = \alpha/n < 0.0025$,
224 where n=20; 10 ROIs x both hemispheres).

225 **fMRI data processing**

226 For each participant, the functional volumes were mapped on the high-resolution anatomical
227 surfaces using FreeSurfer. Surface-based fMRI data processing was then carried out using a
228 standard FS-FAST routine (FreeSurfer's functional analysis stream tool) [Fischl, 2012]. First,
229 preprocessing of the fMRI data was performed that includes the following sequence: template and
230 brain-mask creation, followed by the registration of the functional data with FreeSurfer anatomical
231 structure, motion correction, slice timing correction, intensity normalization of all voxels and time
232 points, resampling of the data to the FreeSurfer average brain (fsaverage) atlas, and spatial
233 smoothing of the data by a 5mm Full-Width/Half-Max (FWHM). Next, first level time series analysis
234 of the data was performed for each participant to remove nuisance variables (i.e., head motion)
235 before computing p-values for a contrast between deviant and standard experimental conditions
236 based on individual participant's time courses with a canonical SPM hemodynamic response
237 function. Later, a random-effects group analysis was performed across participants by using a
238 Generalized Linear Model (GLM) implemented in FreeSurfer [Fischl, 2012], followed by a multiple
239 comparisons correction with the false-discovery rate (FDR, $p<0.05$) [Genovese et al., 2002]
240 method. fMRI data processing steps were carried out for the left hemisphere and right hemisphere
241 separately.

Cortical M/EEG source simulations

Bilateral, anatomically constrained sources were simulated for each participant's cortical surface mainly based on the ROI already used for the time-course analysis. First, each ROI defined on the FreeSurfer average brain was transformed to the individual brain anatomy. For each anatomical ROI, all dipolar sources lying within were uniformly activated with a time-course of a half-sinusoidal wave composed with a base frequency of 5 Hz. The amplitude of each individual dipole was then scaled such that the absolute value summed over all dipoles within a single ROI amounted to 25 nAm peak. The polarity of the sources was assigned as positive- or negative-going for each ROI with reference to the cortical surface. For each ROI, a source in the left and right hemisphere were combined to yield a bilateral source configuration. Only for S1, the simulation was limited to a source in the left hemisphere. To simulate realistic sensor level noise, the individual noise-covariance matrices based on the M/EEG data were used and scaled to a number of 200 averages. The simulations were then analyzed as described above for the experimental data, separately for each ROI used for the simulation. Individual scalp-EEG, sensor-MEG, and cortical dSPM source estimates were computed at the peak of the simulated source for each individual data set and then averaged across all 12 simulated data sets.

Explaining experimental data by simulated activity

Linear combinations of the simulated M/EEG patterns from the previous paragraph were used to explain the scalp/sensor-level M/EEG data. The M/EEG data were averaged across subjects at the individual peak latency of the P3 in EEG electrode Pz and in Cz for the N1. The relative weighting of each simulated ROI component was determined with a least-squares procedure to best explain the M/EEG data. This can be written as:

$$\text{Simulated M/EEG} = \arg\min \left(\Sigma_i W_i\, x_i(n) - y(n)\right)^2 \qquad (3)$$

Where, W is the latent weighting vector for each (bilateral) ROI, x(n) is the ROI-based M/EEG simulation, and y(n) is the P3 (N1) data.

For this procedure, the MEG and EEG data were normalized relative to the standard deviation and mean of the pre-stimulus baseline interval (i.e., MEG and EEG data were transformed to a z score), keeping the relative amplitudes within MEG and EEG data intact. To control for linear dependence, a multi-collinearity test was carried out by calculating the variance-inflation factor (VIF) across the ROI-based M/EEG simulations. VIF cutoff for linear independence was set to 5, i.e., all ROI combinations with a VIF value of less than 5 were considered linearly independent.

To quantify the quality of each model, the residual variance (RV) was calculated between the P3 (N1) data and the weighted combination of ROI-based simulations. The weights provided in the table represent the weight W multiplied by 25 nAm, which was the strength of the summed simulated activity within each source. In this scaling, the weights provide a rough estimate of the source strength underlying the activity in the respective ROIs at the P3 (N1) peak latency. Note that this source strength does not equal the strength of a single dipolar source, since the variable geometry of ROIs cause different degrees of signal cancelation within each multi-dipole source.

Results

A standard auditory oddball paradigm was used with the main goal of providing a high signal-to-noise ratio for source analysis. The paradigm comprised repeated, frequent 1000 Hz standard tones and rare 900 Hz deviants, which participants detected by button press. The average hit rate across subjects in M/EEG was 97±3% and mean reaction time 507±103ms (mean ± standard deviation). In fMRI the hit rate was 99±4% and the reaction time 490±150ms.

At the electrode and sensor levels (Figure 1a), the two most prominent peaks of the event-related response are the central negativity around 100 ms (N1) in both deviants and standards, and the prominent centro-posterior positivity around 400 ms (P3) evoked by deviants (targets). While this P3 is readily evident as the biggest response in the EEG deviant waveforms around 400 ms, the N1 is more prominent in MEG. When averaging is aligned to the onset of the button press instead

(Figure 1b), the EEG shows a slow and steady increase up to about 40 ms after the button press, whereas MEG activity shows a steeper increase right after this event. Thereafter, EEG and MEG similarly show a slow and steady decrease. Maps of the EEG and MEG distribution at the individual maximum at Pz are highly similar when compared between the stimulus- and response-locked versions of the P3, with some differences in the left hemisphere that are more prominent in MEG (Figure 1c).

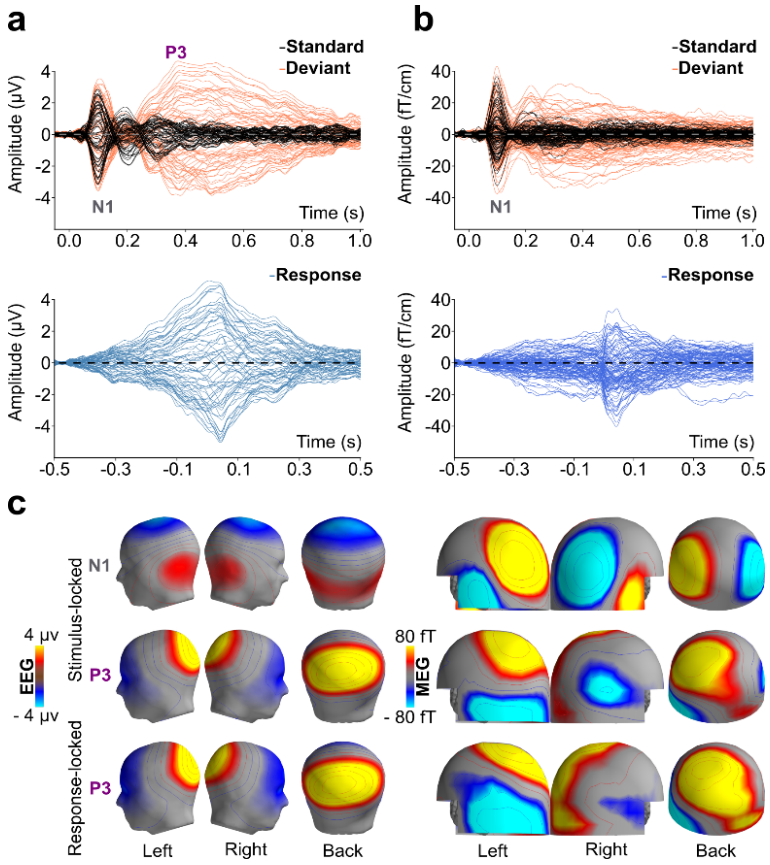

Figure 1 Grand-average evoked-response waveforms and maps. (a) Stimulus-locked EEG waveforms (left) and MEG waveforms (right) for standards (black) and deviants (orange). While the N1 is observed for standards and deviants alike, activity in the P3 time window from 300 – 600 ms is only observed for deviants. (b) Waveforms averaged to the button press for detected deviants. While the EEG (left) is dominated by an increasing signal slightly beyond the button press, the MEG (right) shows a particularly strong, steeply rising response after the button press, corresponding to the somato-sensory feedback. c Grand average EEG maps (upper) and reconstructed MEG magnetometer maps (lower) at the peak latency of the N1 (left), the P3

(middle), and the response-locked P3 (right). Individual peak latencies for mapping were determined at electrode Cz for N1 and at electrode Pz for response-locked P3.

Source analysis of the P3 in comparison to fMRI

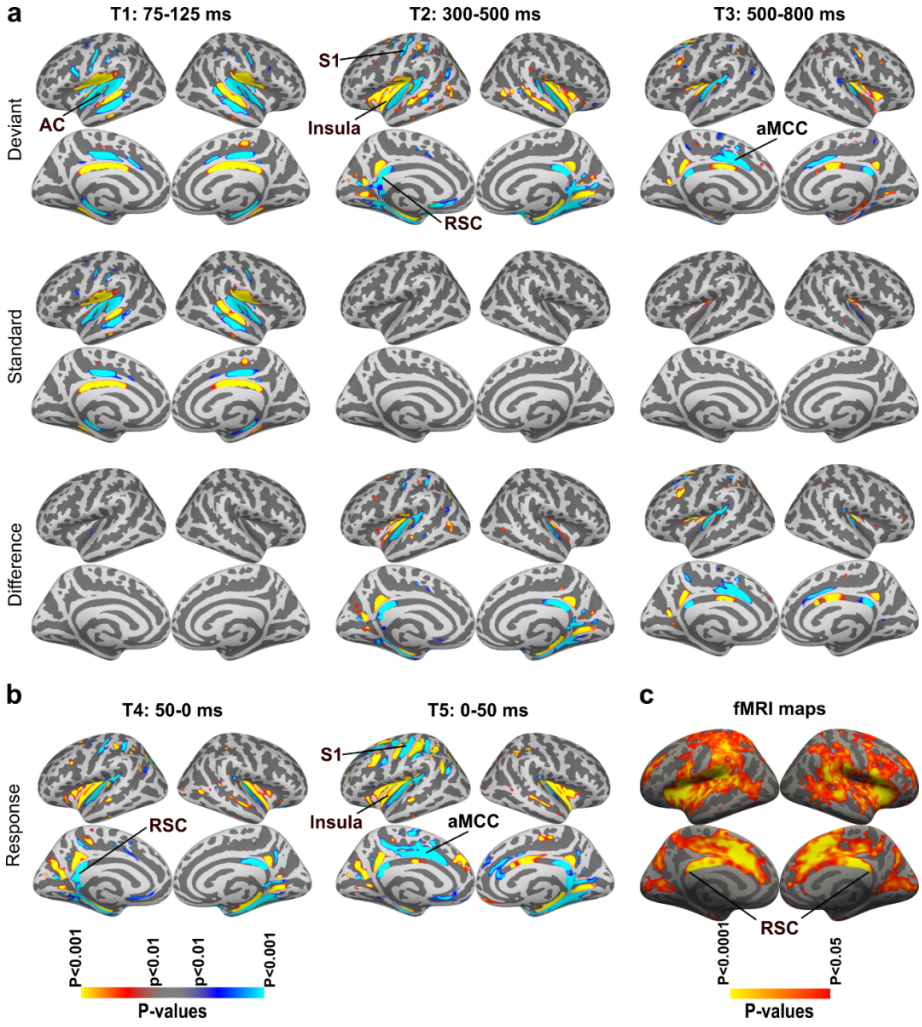

Figure 2 Cortical M/EEG and fMRI activation maps. (a) Combined M/EEG dSPM maps for deviants (upper), standards (middle), and the contrast deviants – standards (lower) in three different time windows (p<0.01). The early 75 – 125 ms time window (T1) is focused on the N1, the middle 300 – 500 ms time window (T2) on the P3, and the late 500 – 800 ms time window (T3) on the late frontal negativity. Because the dSPM maps are based on a fixed-effects statistic, the number of standard trials was reduced to the number of deviant trials

317 for this analysis. (b) dSPM maps for the response-locked average in the time window 50 ms before and 50
318 ms after the button press. (c) fMRI maps for the contrast deviants – standards ($p<0.05$, FDR corrected), based
319 on a random-effects statistic.
320

321 To obtain reliable source models for the P3, the raw M/EEG data were first meticulously pre-
322 processed to exclude, and model known artifact sources. Source analysis of the evoked response
323 was obtained by calculating dynamical statistical parametric maps (dSPM) [Dale et al., 2000] in an
324 individual cortical source space, and a dSPM across subjects was then calculated after morphing
325 the individual source estimates onto the Freesurfer average brain. The results of this procedure are
326 shown in Figure 2a. In the early N1 time range (T1: 75 – 125 ms), source activity is observed in AC
327 on the superior temporal plane with spread to adjacent and medial areas, including the inferior
328 parietal lobes, superior temporal sulcus, medial temporal lobes, and posterior MCC (pMCC). For
329 deviants, AC activity persists into the P3 time range (T2: 300 – 500 ms), but the activation pattern
330 somewhat changes its distribution and extends more anteriorly towards the insular cortex then.
331 Moreover, consistent activation is observed in the retro-splenial cortex (RSC) and in the posterior
332 cingulate cortex (PCC) [Vogt et al., 1995; Vogt, 2019]. The RSC and PCC are opposite to each
333 other, lying on the ventral and dorsal bank of the cingulate gyrus, respectively. Accordingly, the
334 polarity with respect to the cortical surface is positive in PCC and negative in RSC, suggesting that
335 only one of the two is the biophysical generator. This activity continues into the later time window
336 (T3:500 – 800 ms), in which additional activity is observed in anterior MCC (aMCC; previously
337 subsumed to ACC [Vogt et al., 1995; Vogt, 2019]). This aMCC activity is of opposite orientation to
338 PCC/RSC, i.e., negative in the dorsal and positive in the ventral bank of aMCC. Qualitatively similar
339 source analysis results were also obtained by application of other widely used source estimation
340 methods (Figure S1) including standardized low-resolution brain electromagnetic tomography
341 (sLORETA) [Pascual-Marqui R D, 2002] and the unit-noise gain minimum variance beamformer
342 (Borgiotti-Kaplan beamformer) [Sekihara and Nagarajan, 2008].

We also evaluated the activity with respect to the button presses indicating correct target detection (Figure 2b). These response-locked maps overall show similar activation patterns as the stimulus-locked maps in the 50 ms before the button press. In the 50 ms after the button press, as expected, the activity around left S1 is much stronger. No significant motor-cortex activity, peaking before the button press, was observed.

The same auditory oddball paradigm was employed in an fMRI experiment, to directly compare M/EEG and fMRI maps. The fMRI results for the deviant-minus-standard contrast ($p<0.05$, Figure 2c) confirmed previous reports [Bledowski et al., 2004; Kim, 2014] of extensive brain activation for oddball, or generally target detection, with activity in frontal, parietal, and temporal lobes, as well as extensive activation in midline structures around MCC and SMA. When comparing the difference maps for M/EEG (Figure 2a) and fMRI (Figure 2c), it becomes evident that only part of the sites identified by fMRI also show significant source activity in M/EEG, including AC, MCC, S1, and probably insular cortex. Strong fMRI activity is also observed in RSC, but not in PCC. Based on this intramodal comparison, it would therefore appear that the M/EEG activity is also more likely generated in RSC. When the fMRI activity is thresholded more conservatively (Figure S2), it appears that the most robust foci of activity are the RSC, aMCC/SMA, insular cortex, auditory cortex, and TPJ. This pattern is quite similar to the M/EEG source analysis, with the exception of TPJ, where no significant activity was observed in the source analysis.

Source time courses of M/EEG

In order to explore the temporal characteristics of the prominent M/EEG sources in more detail, we calculated source-level time courses for regions of interest (ROI) in the RSC, dorsal aMCC, AC (Heschl's gyrus), insular cortex, and the hand area of S1. As can be observed in these stimulus- and response-locked time courses (Figure 3a and Figure 3b), the ROIs segregate a number of distinct neural processes by their timing. Activity in AC shows the typical N1 waveform. Subsequent to the N1, there is a sustained field that is significant in the deviant-minus-standard comparison on the left. Typical P3-like time courses are observed in RSC and insular cortex, and with longer

latency in aMCC (note that the orientation of the RSC and aMCC sources are opposite to each other and that only the RSC produces a positive-going field at Pz)

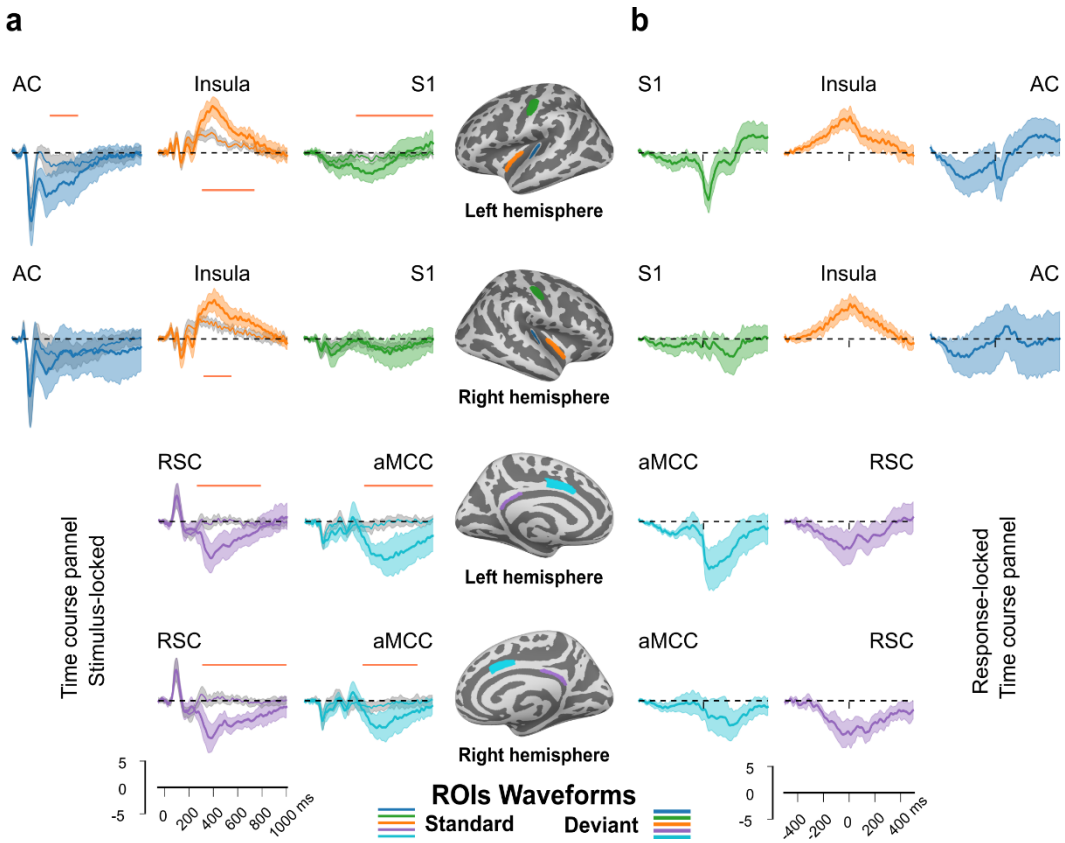

Figure 3 ROI-based source waveforms. Source waveforms based on dSPM, calculated for the ROIs shown in the middle column using the same color code. The ROIs include auditory cortex (AC), anterior insular cortex (insula), primary somatosensory cortex (S1), retro-splenial cortex (RSC), and anterior mid cingulate cortex (aMCC). (a) stimulus-locked source time courses, averaged relative to tone onset. Typical P3 source waveforms are observed in RSC (purple) and insula (orange). The orange bar indicates the time interval in which the deviant and standard responses are significantly different from each other (cluster-based permutation test, see methods for details). (b) response-locked source time courses shown in similar configuration.

An interpretation of the P3 as a build-to-threshold process suggests a response increase until (briefly after) the motor response [O'Connell et al., 2012; Twomey et al., 2015]. The present data

384 show a similar response shape directly at the source level in RSC and insular cortex. Note that the
385 stimulus and response locked variants are of approximately similar amplitude, which is compatible
386 with the hypothesis that the P3 is neither locked to the stimulus nor to the response, but represents
387 a mapping between the two [Asanowicz et al., 2020; Verleger et al., 2014]. In contrast, activity in
388 S1 shows a prominent transient wave that peaks approximately 40 ms after the button press, most
389 likely representing tactile and proprioceptive somatosensory feedback related to the button press.
390 A small transient after the button press is also observed in left AC; the latency of this wave coincides
391 with the activity in S1, suggesting that it is spread from or coactivation with S1 rather than auditory
392 evoked activity related to the button press. Finally, activity in aMCC increases rapidly around the
393 button press and persists for more than 300 ms thereafter, suggesting a closer relationship to the
394 task response than to the auditory stimulus.

395 **Comparison with simulated source data**

396 Next, to evaluate the relationship between neural sources, spread of the source estimates, and
397 scalp/sensor distributions, we simulated (i) the source analysis and (ii) the scalp/sensor distribution
398 that would be generated by activity at the different ROIs based on the individual anatomy of the
399 study participants. Each simulated source had a summed source current of 25 nAm (see methods
400 section for details). As expected, these simulations reproduce the spread that is observed for a
401 focal source to neighboring sulci, for example to the inferior parietal lobe and to the superior
402 temporal sulcus in the case of activity in the primary AC (Figure 4a). Spread from AC is also
403 observed in the medial temporal lobe around the hippocampal gyrus and in the pMCC, matching
404 the activity pattern observed at the peak of the N1 in the original data (Figure 2a). This suggests
405 that the data in the 75 - 125 ms time window can be explained with bilateral sources in AC.
406 Some spread is also observed from AC to insular cortex and vice versa. The positive-going activity
407 in insular cortex is not explained by spread from Heschl's gyrus, however, suggesting that this
408 activity observed in the P3 time window is really generated in insular cortex.

409 To quantify the interaction between the evaluated brain regions in the dSPM source analysis, we
410 calculated the point-spread function and cross-talk function between ROIs (Figure 4c; Figure S3

and Figure S4). A strong interaction between sources within one hemisphere is observed between (1) Heschl's gyrus and hippocampal gyrus, (2) insular cortex and aMCC, and (3) insular cortex and hippocampal gyrus. Strong spread is also observed between RSC and contralateral aMCC. Spread between left S1 and AC is also confirmed by this analysis, which explains the S1-like waveform for response-looked waveforms in AC (Figure 3a). In contrast, there was comparatively little spread between AC and insular cortex ROIs.

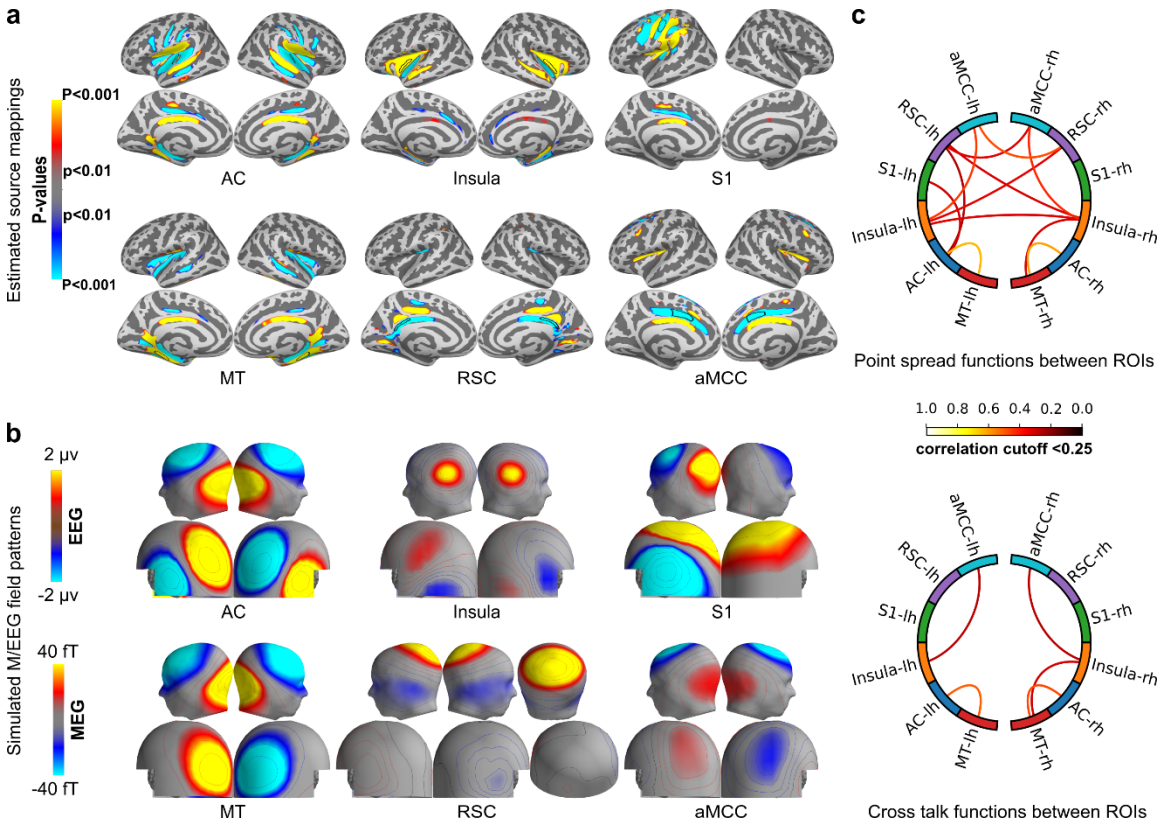

Figure 4 Simulated M/EEG and analysis of spread. (a, b) The data represent an average of n=12 individual simulations, based on bilateral, individually morphed ROIs in auditory cortex (AC), Insula, medial temporal cortex (MT), retrosplenial cortex (RSC), and anterior middle cingulate cortex (aMCC). The simulation of the primary sensory hand area (S1) is based on a single, left sided ROI. Source polarity was chosen to match the pattern observed in the N1 (AC, MT) or P3 (insula, S1, RSC, aMCC) time window shown in Figure 2. (a) dSPM based source mappings of the simulated M/EEG data (p<0.01). (b) Scalp/sensor level maps of the grand-average simulated EEG (upper) and MEG (lower), same scaling for all conditions. (c) Point-spread analysis (upper circle) and cross-talk analysis (lower circle) for the same ROIs used in (a) and (b). Each analysis is

426 visualized using a circular graph with an absolute arbitrary correlation cutoff value of 0.25. The exact values
427 are summarized in Figure S3 (point spread) and Figure S4 (cross-talk).
428
429 The RSC source produces a symmetric, posterior EEG scalp distribution that matches well with
430 main aspects of the typical P3 observed in our data (Figure 1c). In comparison to EEG, the
431 simulated MEG activity for an RSC source is relatively weak, which could be related to the difficulty
432 of recording P3 in MEG reported previously [Siedenberg et al., 1996]. However, the MEG simulation
433 does not match well with the measured MEG map at the P3 peak (Figure 1c). Moreover, the P3-
434 peak maps showed higher reproducibility in EEG at the individual level, and much more variability
435 in MEG (Supplementary Figures 5 and 6). These data indicate that the explanation of the EEG and
436 in particular the MEG data requires multiple sources, for which MEG and EEG supposedly have
437 different sensitivity.
438 **Explaining the P3 with simulated M/EEG data**
439 We therefore explored how the combined M/EEG P3 data can be explained by a combination of
440 the sources that were used for the time-course analysis. To quantify the relative contribution of
441 potential sources, the simulations based on the ROIs used for the time-course analysis were fitted
442 with a least-squares procedure to the P3 data at its peak. The results show that a reasonable
443 explanation of both EEG and MEG data can be achieved with this procedure (Figure 5), leaving
444 6% residual variance in EEG and 62.5% residual variance in MEG (Table 1). Among all five
445 sources, the RSC was scaled to the highest amplitude. When one of the sources was systematically
446 omitted from the model, a massive increase of residual variance in EEG was only observed with
447 the RSC omitted. Note that omitting RSC also led to the strongest increase of residual variance in
448 MEG, supporting that the relatively weak contribution of the RSC is still relevant for MEG. All other
449 sources only caused weak increment of the residual variance in EEG when omitted. This was also
450 the case for the S1 source, the omittance of which increased the residual variance by only 0.4% in
451 EEG, but by 19% in MEG, demonstrating that this source is almost as important for the MEG maps
452 as the RSC at the P3 peak.

To test the validity of the modeling approach, the same sources were fitted to the N1 data, leading to zero weights for all sources except for AC and insula (Figure 5; Table S1). This model resulted in a residual variance of 16.3% in EEG and 27.8% in MEG. While the weighting of the insular cortex of about 1/3 of the auditory cortex appears relatively high, leaving out the insular ROI leads only to a minor increase of the residual variance, whereas the insular cortex alone cannot explain the N1 data well.

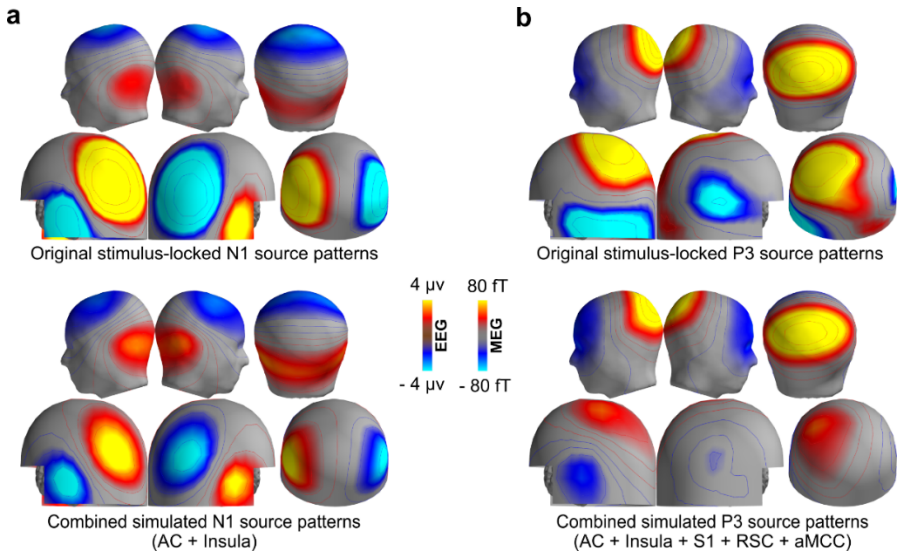

Figure 5 Multi-source simulation for the stimulus-locked N1 and P3. (a) Grand average EEG maps and reconstructed MEG magnetometer maps at the peak latency of the N1 in EEG (upper). Combined simulation of N1 maps in scalp/sensor space based on the sum of the sources (AC and insula; see Table S1) fitted to the stimulus-locked N1 (lower). (b) Grand average EEG maps and reconstructed MEG magnetometer maps at the peak latency of the P3 in EEG (upper). Combined simulation of P3 maps in scalp/sensor space based on the sum of the sources (AC, insula, S1, RSC, and aMCC; see Table 1) fitted to the stimulus-locked P3 (lower).

Note that the values of the residual variance of these models must not be directly compared between MEG and EEG. First, higher residual variance in MEG is generally expected based on the more focal signal in planar gradiometers, which leaves other sensors with less signal but similar noise. Second, the relative weighting of MEG and EEG is based on Z-scores, which then results in

472 an advantage for EEG because of higher signal to noise level. The relative amplitude of MEG and
473 EEG simulations depends on assumptions made in the head model, in particular the conductivity
474 of the EEG model, which is individually different and difficult to estimate exactly. As a consequence,
475 the amplitude of the MEG is somewhat underestimated by the model, for both N1 and P3, which is
476 an additional source of higher residual variance in MEG compared to EEG.

477

478 **Table 1** Modeling the grand-average P3 data with simulated M/EEG based on anatomically defined
479 source regions (Figure 4b).

	Simulated source activation patterns					**Residual variance (RV) (%)**	
Source strength (nAm)	**AC**	**Insula**	**S1**	**RSC**	**aMCC**	**EEG**	**MEG**
	5.50	7.75	11.25	44.25	12.75	6.0	62.50
	-	3.0	12.75	42.0	20.25	6.0	65.30
	3.50	-	11.75	42.0	17.75	5.0	67.0
	9.25	11.25	-	49.75	16.25	6.40	81.50
	0.0	0.0	22.75	-	4.0	52.90	87.10
	10.25	15.50	12.0	45.0	-	8.30	60.50

480

481 Finally, we tested two previous hypotheses for the generation of P3, which were not suggested by
482 the dSPM analysis. First, a source in TPJ has been suggested based on fMRI, fMRI-constrain
483 EEG, and lesion studies [Bledowski et al., 2004; Knight et al., 1989]. To this end, we used the
484 region provided by a standard parcellation [Destrieux et al., 2010]. Such a bilateral TPJ source
485 produces a bilateral posterior maximum (Figure S7b), but cannot replace the RSC in direct

comparison. When added as the sixth source to the model from Table 1, TPJ receives no weight. When TPJ is used to replace RSC in a model with five sources, the residual variance increases to 50.4% in EEG and 85.4% in MEG, providing no support for a relevant contribution of TPJ to the P3 in the present data.

Second, a previous EEG study suggested that a distributed source in superior parietal cortex [Moores et al., 2003] could explain the P3. For this simulation, it was assumed that a distributed source existed right below the centro-posterior P3 in the EEG map, extending down to the IPS with a homogeneous amplitude distribution. This extended source indeed produces an EEG pattern with considerable similarity to the centro-posterior P3 (Figure S7b), as well as to the RSC simulation. Replacing the RSC with this distributed source accordingly produces only slightly higher residual variance in comparison (Table S2). It is interesting to note that the dSPM estimate of this simulated source shows considerable spread to the RSC and PCC (Figure S7a), but, conversely, no strong activity in parietal sulci was observed in the P3 source analysis, as would have been predicted by this simulation.

Discussion

Our results provide evidence of a role for RSC [Vogt et al., 1995; Vogt, 2019] in the generation of the classical P3. A second source with a typical P3 time course was observed in insular cortex, but this component was not dominant for the M/EEG maps. Other sources like S1, AC and aMCC are active in an overlapping time range but contribute to different aspects of the evoked response, which we do not consider part of the classical P3. This model is at odds with the long-held assumption that the P3 as observed by M/EEG is generated by a more distributed set of sources [Bledowski et al., 2004; Mulert et al., 2004b] that is not well accessible to source analysis techniques. The results are based on the combination of EEG, MEG, and individual anatomy to provide the best possible information for the source analysis [Molins et al., 2008]. Conversely, we did not directly constrain the source analysis with information from fMRI [Bledowski et al., 2004]. In

our view, caution is warranted when using such priors unless correlation between the brain activity measured by the different modalities has been independently confirmed; otherwise, such priors have the potential to mislead M/EEG analyses and lead to incorrect inferences regarding M/EEG sources. Indirectly, however, we used the information provided by fMRI, which first confirms that the RSC is active during target detection, and second allows for the disambiguation of the ventral RSC from the dorsal PCC, an inference that cannot be easily made based on the M/EEG data alone.

The limitations of the inverse problem remain, though, and alternative source models can easily be constructed. For example, an extended positive-going source directly below the P3 maximum in the EEG map produced a very similar map and could be used to substitute the RSC source in our model. A previous EEG study that used minimum-norm source reconstruction without noise normalization had proposed such a solution [Moores et al., 2003]. However, the latter method generally prefers superficial sources [Lin et al., 2006b], which is balanced by noise normalization as used in the present study. One further difficulty of M/EEG source analysis is that, in contrast to fMRI, the distribution of a source is not directly related to the actual extent of the activity on the cortex. The pattern with opposite polarity with respect to the (outward) cortical normal in adjacent banks of a sulcus is often caused by spread of a focal source (Figure 4b), whereas a physiological source that extends across both banks with the same polarity would lead to major signal cancelation for distant recordings in M/EEG [Goldenholz et al., 2009]. We therefore chose to display source activity together with polarity information, to avoid the impression of extended sources where they are unlikely, based on the activation pattern, and estimated the spread and activation pattern of each source by simulation studies.

The other limitation is the degree to which fMRI can be used to constrain M/EEG source analysis. All sources that were found active in the dSPM maps of this study were also confirmed by fMRI, but fMRI shows activity in additional areas that were not revealed by M/EEG source analysis. There are at least two potential sources for this discrepancy: First, electric activity of similar surface polarity cancels out for M/EEG if the source spans two sides of a sulcus [Ahlfors et al., 2010],

539 whereas this configuration would rather support the activity's detection in fMRI. This could e.g.,
540 apply to potential sources in the IPS or TPJ; it could then be that there was another P3 source in
541 this region, but that its signal-to-noise ratio was low for M/EEG. Second, fMRI often does not match
542 with low-frequency M/EEG activity in the delta and theta band such as e.g. the error-related
543 negativity [Agam et al., 2011], but better with neural activity in the gamma band [Logothetis et al.,
544 2001; Niessing et al., 2005; Steinmann and Gutschalk, 2011]. Thus, while the strong RSC activity
545 in fMRI generally supports the RSC's contribution to the P3 source, it still remains possible that the
546 relationship between M/EEG and fMRI activity in this region is indirect, e.g., via functionally coupled
547 gamma activity.

548 Activity in the PCC and RSC has also been reported in intracranial recordings of the P3 [Halgren
549 et al., 1995b], without providing a clear separation between the two. While the authors of that study
550 suggested that the PCC/RSC was a source of the P3a rather than the P3b, neither fMRI [Kim,
551 2014] nor source-analysis studies [Bledowski et al., 2004] have confirmed such a strict separation
552 of P3 subcomponents as suggested based on these intracranial data. As a limitation, while the
553 depth recordings found high amplitudes in and near PCC, no polarity reversal was found [Halgren
554 et al., 1995b], which would have confirmed that the electrode passed through the source.

555 Another constraint for a potential P3 source in RSC is how this region is connected to other brain
556 networks recruited by target processing. The PCC has been demonstrated to be a major hub of the
557 “task-negative” default-mode network [Fox et al., 2005], while activation during oddball detection
558 [Kim, 2014] has been observed in “task-positive” networks [Fox et al., 2005; Hugdahl et al., 2015]
559 such as the dorsal and ventral attention networks [Yeo et al., 2011]. In the early resting-state
560 network studies, PCC activation included all of RSC [Fox et al., 2005], whereas later, more detailed
561 network maps [Yeo et al., 2011] segregated the dorsal part of RSC into a fronto-parietal network,
562 which would better match with a role in active target detection. Anatomical studies in monkeys
563 indicate that both PCC and RSC are reciprocally connected with multiple frontoparietal areas that
564 are active during oddball tasks in fMRI [Kobayashi and Amaral, 2007; Vogt and Pandya, 1987].
565 This would be consistent with the idea that even if the fronto-parietal network does not itself

566 generate the P3, it may still be functionally coupled with a generator in RSC. Such connectivity
567 would explain previous findings of reduced P3 with right-TPJ lesions [Knight et al., 1989; Verleger
568 et al., 1994], even if TPJ was not the source of P3. In fact, a model where TPJ provides input into
569 RSC, the neuroelectric source of P3, could better explain why unilateral TPJ lesions caused
570 bilateral reduction of the P3 [Knight et al., 1989].

571 The RSC is also functionally coupled to the hippocampus in the medial temporal lobe [Alexander
572 et al., 2018]. Given the hippocampal P3-like activity demonstrated by iEEG [Halgren et al., 1980],
573 this raises the possibility of a close functional coupling between the extracranial P3 in M/EEG and
574 the intracranial hippocampal activity, despite their anatomical dissociation. Another important
575 question for the source analysis and simulation studies was if hippocampal P3-like activity could
576 potentially be recorded in M/EEG. Despite its clear demonstration in iEEG [Halgren et al., 1980],
577 no hippocampal activity has been shown in fMRI in this (Figure 2c) or previous odd-ball-paradigm
578 fMRI studies [Kim, 2014]. One possible reason for this negative finding could be different neuro-
579 vascular coupling in medial temporal lobe compared to neocortex [Hill et al., 2021], suggested
580 recently based on combined iEEG and fMRI. While the contribution of a hippocampal source to the
581 parietal P3 in EEG had already been excluded based on lesion studies [Johnson, 1988; Onofrj et
582 al., 1992], this does not exclude that hippocampal activity may generally contribute to other aspects
583 of the M/EEG response [Alberto et al., 2021], even though with only a weak signal-to-noise ratio.
584 Indeed, the mapping shown in Figure 2 also suggests activity in the medial temporal lobe. However,
585 this activity was as prominent in the N1 as in the P3 time interval, which is not consistent with
586 known iEEG time courses in hippocampus [Halgren et al., 1980]. Moreover, we demonstrated that
587 there is considerable spread and crosstalk between the medial temporal lobe and AC as well as
588 insular cortex (Figure 4). It is therefore more likely that the activity observed in the medial temporal
589 lobe in our source analysis represents spread from AC and insular cortex, particularly given the
590 fact that M/EEG signal-to-noise ratio is much higher in AC (and somewhat higher in insular cortex)
591 than in the hippocampus [Goldenholz et al., 2009]. This leaves us with the paradoxical situation
592 that there is strong iEEG evidence for P3-like activity in the hippocampus evoked by the paradigm

593 used [Halgren et al., 1980], but that this activity is hard to detect or to distinguish from other sources
594 with all three non-invasive techniques used in this study.

595 The situation is somewhat different for the insula. While there is also spread from AC to the insula
596 (or its vicinity) in the N1 time interval, the pattern is clearly different in the P3 time interval, with
597 surface-positive activity in the insular cortex; activity in AC remains surface negative in this time
598 interval, as reported previously for a passive oddball paradigm [Kretzschmar and Gutschalk, 2010].
599 We therefore consider it more likely that the P3-like time course shown in Figure 3 is generated in
600 the insula, rather than in the temporal lobe. P3 generators in the insula have been suggested
601 before. An EEG study [Bledowski et al., 2004] suggested a contribution of insular cortex to the P3a.
602 A recent iEEG study demonstrated a stronger P3b in anterior insular cortex [Citherlet et al., 2020],
603 in synchrony with gamma activity in the same latency range. Given the observation of strong fMRI
604 activity for detected oddballs in insular cortex, this supports the hypothesis stated above that
605 gamma is a potential link between the P3 and BOLD activity. Finally, strong fMRI activity was
606 observed in aMCC. Insular and aMCC activity are often observed together in fMRI [Yeo et al.,
607 2011], but the time course of the insula and aMCC found here are quite different: the insular time
608 course is similar to the RSC and shows a build-up towards the time of the button press. In contrast,
609 aMCC activity was most prominent after the button press and may thus rather indicate some kind
610 of performance control [Heilbronner and Platt, 2013].

611 At this point, this source analysis is limited to a single paradigm, the classical auditory oddball
612 paradigm. The dominant component in this paradigm is the P3b, but it can be expected that some
613 P3a source activity will also be present. Therefore, we cannot as yet make strong conclusions with
614 respect to the neural sources of these subcomponents. The EEG distribution of the simulated
615 bilateral RSC source over centro-parietal electrodes, however, makes it a better fit for the P3b
616 rather than the P3a [Polich, 2007]. If other sources are more specific for the P3a [Halgren et al.,
617 1995a] or show strong overlap between these two subcomponents [Kim, 2014] will require further
618 studies that manipulate the relative strength of these components. Other, more complex tasks will
619 certainly be expected to involve additional brain regions. While we propose that the P3 generator

in RSC will remain a constant contributor for such paradigms as well, this hypothesis requires evaluation in future experiments or the reevaluation of existing data.

Conclusion

Multiple neural processes are active in parallel with the P3 in M/EEG, some observed more easily with fMRI and some more easily with EEG or MEG. But while the P3 is most likely functionally coupled to this distributed neural network, it does not appear to be the bioelectric source of the classical, parietal P3 signal measured in EEG. Based on the evidence presented here, this source appears to be more focal and to lie in the RSC. This finding is essential to explore the functional role of the P3 between the fronto-parietal network observed in fMRI [Kim, 2014] and the hippocampal P3-like activity demonstrated with iEEG [Halgren et al., 1980], and will help to better understand the functional roles of both RSC and the P3. Moreover, understanding its functional anatomy may support the application of the P3 as diagnostic tool. For example, reduced P3 in Alzheimer's disease [Frodl et al., 2002] might be linked to cortical hypometabolism and tau accumulation [Strom et al., 2022], the latter of which has been suggested to covary with the connectivity between RSC and hippocampus [Ziontz et al., 2021]. We hope that future invasive studies will seek to confirm the source configuration suggested by this non-invasive study, possibly by demonstrating co-occurrence of (high-)gamma activity together with a typical P3 time course in RSC.

Author contributions

Diptyajit Das: Conceptualization, Formal Analysis, Data Curation, Visualization, Writing - Original Draft; **Marnie E. Shaw:** Conceptualization, Investigation, Writing - Review & Editing; **Matti S. Hämäläinen:** Validation, Writing - Review & Editing; **Andrew R. Dykstra:** Validation, Writing - Review & Editing; **Laura Doll:** Validation, Writing - Review & Editing; **Alexander Gutschalk:** Conceptualization, Supervision, Validation, Writing - Original Draft & Editing, Funding acquisition.

Acknowledgements

This work was primarily supported by Deutsche Forschungsgemeinschaft grant DFG 593/5-1 (AG) and Bundesministerium für Bildung und Forschung grant 01EV0712 (AG), as well as by National Institutes of Health grants R01NS104585 and P41EB030006 (MSH).

Conflict of interest statement

The authors declare no competing financial interests.

Data availability

The processed M/EEG and fMRI data and scripts will be made available on heiDATA, the open research data repository of Heidelberg University under the following doi (not yet published): https://doi.org/10.11588/data/YB9SQI

References

Agam Y, Hämäläinen MS, Lee AKC, Dyckman KA, Friedman JS, Isom M, Makris N, Manoach DS (2011): Multimodal neuroimaging dissociates hemodynamic and electrophysiological correlates of error processing. Proc Natl Acad Sci U S A 108:17556–17561.

Ahlfors SP, Han J, Lin FH, Witzel T, Belliveau JW, Hämäläinen MS, Halgren E (2010): Cancellation of EEG and MEG signals generated by extended and distributed sources. Hum Brain Mapp 31:140–149. http://www.ncbi.nlm.nih.gov/pubmed/19639553.

Alberto GE, Stapleton-Kotloski JR, Klorig DC, Rogers ER, Constantinidis C, Daunais JB, Godwin DW (2021): MEG source imaging detects optogenetically-induced activity in cortical and subcortical networks. Nat Commun 12:5259. http://dx.doi.org/10.1038/s41467-021-25481-y.

Alexander AS, Rangel LM, Tingley D, Nitz DA (2018): Neurophysiological signatures of temporal

coordination between retrosplenial cortex and the hippocampal formation. Behav Neurosci 132:453–468.

Asanowicz D, Gociewicz K, Marcin K, Finc K, Bonna K, Cleeremans A, Binder M (2020): The response relevance of visual stimuli modulates the P3 component and the underlying sensorimotor network:1–20.

Besl PJ, McKay ND (1992): A method for registration of 3D shapes. IEEE Trans Pattern Anal Mach Intell 14:239–256.

Bledowski C, Prvulovic D, Hoechstetter K, Scherg M, Wibral M, Goebel R, Linden DEJ (2004): Localizing P300 generators in visual target and distractor processing: a combined event-related potential and functional magnetic resonance imaging study. J Neurosci 24:9353–9360. http://www.ncbi.nlm.nih.gov/entrez/query.fcgi?cmd=Retrieve&db=PubMed&dopt=Citation&list_uids=15496671.

Chaudhary U, Birbaumer N, Ramos-Murguialday A (2016): Brain-computer interfaces for communication and rehabilitation. Nat Rev Neurol 12:513–525.

Citherlet D, Boucher O, Tremblay J, Robert M, Gallagher A, Bouthillier A, Lepore F, Nguyen DK (2020): Spatiotemporal dynamics of auditory information processing in the insular cortex: an intracranial EEG study using an oddball paradigm. Brain Struct Funct 225:1537–1559. https://doi.org/10.1007/s00429-020-02072-z.

Dale a M, Fischl B, Sereno MI (1999): Cortical surface-based analysis. I. Segmentation and surface reconstruction. Neuroimage 9:179–194. http://www.ncbi.nlm.nih.gov/entrez/query.fcgi?cmd=Retrieve&db=PubMed&dopt=Citation&list_uids=9931268.

Dale AM, Liu AK, Fischl BR, Buckner RL, Belliveau JW, Lewine JD, Halgren E (2000): Dynamic Statistical Parametric Mapping. Neuron 26:55–67.

Destrieux C, Fischl B, Dale A, Halgren E (2010): Automatic parcellation of human cortical gyri and sulci using standard anatomical nomenclature. Neuroimage 53:1–15. http://dx.doi.org/10.1016/j.neuroimage.2010.06.010.

Engemann DA, Gramfort A (2015): Automated model selection in covariance estimation and spatial whitening of MEG and EEG signals. Neuroimage 108:328–342. http://dx.doi.org/10.1016/j.neuroimage.2014.12.040.

Ernst MD (2004): Permutation methods: A basis for exact inference. Stat Sci 19:676–685.

Fischl B, Sereno MI, Tootell RBH, Dale a M (1999): High-resolution inter-subject averaging and a surface-based coordinate system. Hum Brain Mapp 8:272–284.

Fischl B (2012): FreeSurfer. Neuroimage 62:774–781.

Fox MD, Snyder AZ, Vincent JL, Corbetta M, Van Essen DC, Raichle ME (2005): The human brain is intrinsically organized into dynamic, anticorrelated functional networks. Proc Natl Acad Sci U S A 102:9673–8. http://www.pubmedcentral.nih.gov/articlerender.fcgi?artid=1157105&tool=pmcentrez&rendertype=abstract.

Frodl T, Hampel H, Juckel G, Bürger K, Padberg F, Engel RR, Möller HJ, Hegerl U (2002): Value of event-related P300 subcomponents in the clinical diagnosis of mild cognitive impairment and Alzheimer's disease. Psychophysiology 39:175–181.

Genovese CR, Lazar NA, Nichols T (2002): Thresholding of statistical maps in functional neuroimaging using the false discovery rate. Neuroimage 15:870–878.

Goldenholz DM, Ahlfors SP, Hämäläinen MS, Sharon D, Ishitobi M, Vaina LM, Stufflebeam SM (2009): Mapping the signal-to-noise-ratios of cortical sources in magnetoencephalography and electroencephalography. Hum Brain Mapp 30:1077–1086.

Gramfort A, Luessi M, Larson E, Engemann DA, Strohmeier D, Brodbeck C, Goj R, Jas M, Brooks T, Parkkonen L, Hämäläinen M (2013): MEG and EEG data analysis with MNE-

Python. Front Neurosci 7:1–13.

Halgren E, Baudena P, Clarke JM, Heit G, Liégeois C, Chauvel P, Musolino a (1995a): Intracerebral potentials to rare target and distractor auditory and visual stimuli. I. Superior temporal plane and parietal lobe. Electroencephalogr Clin Neurophysiol 94:191–220.

Halgren E, Baudena P, Clarke JM, Heit G, Marinkovic K, Devaux B, Vignal JP, Biraben a (1995b): Intracerebral potentials to rare target and distractor auditory and visual stimuli. II. Medial, lateral and posterior temporal lobe. Electroencephalogr Clin Neurophysiol 94:229–250.

Halgren E, Squires NK, Wilson CL, Rohrbaugh JW, Babb TL (1980): Endogenous potentials generated in the human hippocampal formation and amygdala by infrequent events. Science (80-) 210:803–805.

Hämäläinen MS, Sarvas J (1989): Realistic conductivity geometry model of the human head for interpretation of neuromagnetic data. IEEE Trans Biomed Eng 36:165–171. http://www.ncbi.nlm.nih.gov/entrez/query.fcgi?cmd=Retrieve&db=PubMed&dopt=Citation&list_uids=2917762.

Hamilton HK, Boos AK, Mathalon DH (2020): Electroencephalography and Event-Related Potential Biomarkers in Individuals at Clinical High Risk for Psychosis. Biol Psychiatry 88:294–303. https://doi.org/10.1016/j.biopsych.2020.04.002.

Hauk O, Wakeman DG, Henson R (2011): Comparison of noise-normalized minimum norm estimates for MEG analysis using multiple resolution metrics. Neuroimage 54:1966–1974. http://dx.doi.org/10.1016/j.neuroimage.2010.09.053.

Heilbronner SR, Platt ML (2013): Causal evidence of performance monitoring by neurons in posterior cingulate cortex during learning. Neuron 80:1384–1391. http://dx.doi.org/10.1016/j.neuron.2013.09.028.

Hill PF, Seger SE, Yoo H Bin, King DR, Wang DX, Lega BC, Rugg MD (2021): Distinct

745 neurophysiological correlates of the fMRI BOLD signal in the hippocampus and neocortex. J
746 Neurosci 41:6343–6352.

747 Hillyard SA, Squires KC, Bauer JW, Lindsay PH (1971): Evoked potential correlates of auditory
748 signal detection. Science 172:1357–1360.
749 http://www.ncbi.nlm.nih.gov/entrez/query.fcgi?cmd=Retrieve&db=PubMed&dopt=Citation&li
750 st_uids=5580218.

751 Hugdahl K, Raichle ME, Mitra A, Specht K (2015): On the existence of a generalized non-specific
752 task- dependent network. Front Hum Neurosci 9:1–15.

753 Hyvärinen A (1999): Fast and robust fixed-point algorithms for independent component analysis.
754 IEEE Trans Neural Networks 10:626–634.

755 Jas M, Engemann DA, Bekhti Y, Raimondo F, Gramfort A (2017): Autoreject: Automated artifact
756 rejection for MEG and EEG data. Neuroimage 159:417–429.
757 https://doi.org/10.1016/j.neuroimage.2017.06.030.

758 Johnson R (1988): Scalp-recorded p300 activity in patients following unilateral temporal
759 lobectomy. Brain 111:1517–1529.

760 Kim H (2014): Involvement of the dorsal and ventral attention networks in oddball stimulus
761 processing: A meta-analysis. Hum Brain Mapp 35:2265–84.
762 http://www.ncbi.nlm.nih.gov/pubmed/23900833.

763 Knight RT, Scabini D, Woods DL, Clayworth CC (1989): Contributions of temporal-parietal
764 junction to the human auditory P3. Brain Res 502:109–116.

765 Kobayashi Y, Amaral DG (2007): Macaque monkey retrosplenial cortex: III. cortical efferents. J
766 Comp Neurol 502:810–833.

767 Kretzschmar B, Gutschalk A (2010): A sustained deviance response evoked by the auditory
768 oddball paradigm. Clin Neurophysiol 121.

769 Larson E, Taulu S (2018): Reducing Sensor Noise in MEG and EEG Recordings Using

Oversampled Temporal Projection. IEEE Trans Biomed Eng 65:1002–1013.

Li F, Tao Q, Peng W, Zhang T, Si Y, Zhang Y, Yi C, Biswal B, Yao D, Xu P (2020): Inter-subject P300 variability relates to the efficiency of brain networks reconfigured from resting- to task-state: Evidence from a simultaneous event-related EEG-fMRI study. Neuroimage 205:116285. https://doi.org/10.1016/j.neuroimage.2019.116285.

Lin FH, Belliveau JW, Dale AM, Hamalainen MS (2006a): Distributed current estimates using cortical orientation constraints. Hum Brain Mapp 27:1–13. http://www.ncbi.nlm.nih.gov/entrez/query.fcgi?cmd=Retrieve&db=PubMed&dopt=Citation&list_uids=16082624.

Lin FH, Witzel T, Ahlfors SP, Stufflebeam SM, Belliveau JW, Hamalainen MS (2006b): Assessing and improving the spatial accuracy in MEG source localization by depth-weighted minimum-norm estimates. Neuroimage 31:160–171. http://www.ncbi.nlm.nih.gov/entrez/query.fcgi?cmd=Retrieve&db=PubMed&dopt=Citation&list_uids=16520063.

Linden DE, Prvulovic D, Formisano E, Vollinger M, Zanella FE, Goebel R, Dierks T (1999): The functional neuroanatomy of target detection: an fMRI study of visual and auditory oddball tasks. Cereb Cortex 9:815–823. http://www.ncbi.nlm.nih.gov/entrez/query.fcgi?cmd=Retrieve&db=PubMed&dopt=Citation&list_uids=10601000.

Logothetis NK, Pauls J, Augath M, Trinath T, Oeltermann a (2001): Neurophysiological investigation of the basis of the fMRI signal. Nature 412:150–157. http://www.ncbi.nlm.nih.gov/entrez/query.fcgi?cmd=Retrieve&db=PubMed&dopt=Citation&list_uids=11449264.

Maris E, Oostenveld R (2007): Nonparametric statistical testing of EEG- and MEG-data. J Neurosci Methods 164:177–190.

Molins A, Stufflebeam SM, Brown EN, Hämäläinen MS (2008): Quantification of the benefit from integrating MEG and EEG data in minimum ℓ2-norm estimation. Neuroimage 42:1069–1077.

Moores KA, Clark CR, Hadfield JLM, Brown GC, Taylor DJ, Fitzgibbon SP, Lewis AC, Weber DL, Greenblatt R (2003): Investigating the generators of the scalp recorded visuo-verbal P300 using cortically constrained source localization. Hum Brain Mapp 18:53–77.

Mulert C, Pogarell O, Juckel G, Rujescu D, Giegling I, Rupp D, Mavrogiorgou P, Bussfeld P, Gallinat J, Möller HJ, Hegerl U (2004a): The neural basis of the P300 potential: Focus on the time-course of the underlying cortical generators. Eur Arch Psychiatry Clin Neurosci 254:190–198.

Mulert C, Jäger L, Schmitt R, Bussfeld P, Pogarell O, Möller HJ, Juckel G, Hegerl U (2004b): Integration of fMRI and simultaneous EEG: Towards a comprehensive understanding of localization and time-course of brain activity in target detection. Neuroimage 22:83–94.

Niessing J, Ebisch B, Schmidt KE, Niessing M, Singer W, Galuske R a W (2005): Hemodynamic signals correlate tightly with synchronized gamma oscillations. Science (80-) 309:948–951. http://www.ncbi.nlm.nih.gov/entrez/query.fcgi?cmd=Retrieve&db=PubMed&dopt=Citation&list_uids=16081740.

O'Connell RG, Dockree PM, Kelly SP (2012): A supramodal accumulation-to-bound signal that determines perceptual decisions in humans. Nat Neurosci 15:1729–1735.

Onofrj M, Fulgente T, Nobilio D, Malatesta G, Bazzano S, Colamartino P, Gambi D (1992): P3 recordings in patients with bilateral temporal lobe lesions. Neurology 42:1762–1767.

Pascual-Marqui R D (2002): Standardized low resolution brain electromagnetic tomography (sLORETA): technical details. Methods Find Exp Clin Pharmacol 24:5–12. http://www.keyinst.unizh.ch/loreta.htm.

Peirce JW (2007): PsychoPy-Psychophysics software in Python. J Neurosci Methods 162:8–13. http://dx.doi.org/10.1016/j.jneumeth.2006.11.017.

Polich J (2007): Updating P300: An integrative theory of P3a and P3b. Clin Neurophysiol 118:2128–2148.

Ritter W, Simson R, Vaughan HG (1972): Association cortex potentials and reaction time in auditory discrimination. Electroencephalogr Clin Neurophysiol 33:547–555.

Rogers RL, Basile LFH, Papanicolaou AC, Eisenberg HM (1993): Magnetoencephalography reveals two distinct sources associated with late positive evoked potentials during visual oddball task. Cereb Cortex 3:163–169.

Sekihara K, Nagarajan SS (2008): Adaptive Spatial Filters for Electromagnetic Brain Imaging. Series in. Springer, Berlin; Heidelberg.

Sergent C, Baillet S, Dehaene S (2005): Timing of the brain events underlying access to consciousness during the attentional blink. Nat Neurosci 8:1391–1400.

Siedenberg R, Goodin DS, Aminoff MJ, Rowley HA, Roberts TPL (1996): Comparison of late components in simultaneously recorded event-related electrical potentials and event-related magnetic fields. Electroencephalogr Clin Neurophysiol 99:191–197.

Squires NK, Squires KC, Hillyard SA (1975): Two varieties of long-latency positive waves evoked by unpredictable auditory stimuli in man. Electroencephalogr Clin Neurophysiol 38:387–401. http://www.ncbi.nlm.nih.gov/entrez/query.fcgi?cmd=Retrieve&db=PubMed&dopt=Citation&list_uids=46819.

Steinmann I, Gutschalk A (2011): Potential fMRI correlates of 40-Hz phase locking in primary auditory cortex, thalamus and midbrain. Neuroimage 54:495–504. http://www.ncbi.nlm.nih.gov/pubmed/20688174.

Strom A, Iaccarino L, Edwards L, Lesman-Segev OH, Soleimani-Meigooni DN, Pham J, Baker SL, Landau SM, Jagust WJ, Miller BL, Rosen HJ, Gorno-Tempini ML, Rabinovici GD, La Joie R (2022): Cortical hypometabolism reflects local atrophy and tau pathology in symptomatic Alzheimer's disease. Brain 145:713–728.

845 Sutton S, Braren M, Zubin J, E. R. John (1965): Evoked-Potential Correlates of Stimulus
846 Uncertainty. Science (80-) 150:1187–8.

847 Tarkka IM, Stokić DS, Basile LF, Papanicolaou a C (1995): Electric source localization of the
848 auditory P300 agrees with magnetic source localization. Electroencephalogr Clin
849 Neurophysiol 96:538–545.

850 Twomey DM, Murphy PR, Kelly SP, O'Connell RG (2015): The classic P300 encodes a build-to-
851 threshold decision variable. Eur J Neurosci 42:1636–43.
852 http://www.ncbi.nlm.nih.gov/pubmed/25925534.

853 Uutela K, Taulu S, Hämäläinen M (2001): Detecting and correcting for head movements in
854 neuromagnetic measurements. Neuroimage 14:1424–1431.

855 Verleger R, Heide W, Butt C, Kömpf D (1994): Reduction of P3b in patients with temporo-parietal
856 lesions. Brain Res Cogn Brain Res 2:103–116.

857 Verleger R (2020): Effects of relevance and response frequency on P3b amplitudes: Review of
858 findings and comparison of hypotheses about the process reflected by P3b.
859 Psychophysiology 57:1–22.

860 Verleger R, Metzner MF, Ouyang G, Śmigasiewicz K, Zhou C (2014): Testing the stimulus-to-
861 response bridging function of the oddball-P3 by delayed response signals and residue
862 iteration decomposition (RIDE). Neuroimage 100:271–280.

863 Vogt BA (2019): The cingulate cortex in neurologic diseases: History, Structure, Overview.
864 Handbook of Clinical Neurology 1st ed. Elsevier B.V. Vol. 166.
865 http://dx.doi.org/10.1016/B978-0-444-64196-0.00001-7.

866 Vogt BA, Nimchinsky EA, Vogt LJ, Hof PR (1995): Human cingulate cortex: Surface features, flat
867 maps, and cytoarchitecture. J Comp Neurol 359:490–506.

868 Vogt BA, Pandya DN (1987): Cingulate cortex of the rhesus monkey: II. Cortical afferents. J
869 Comp Neurol 262:271–289.

870 Yamaguchi S, Knight RT (1991): Anterior and posterior association cortex contributions to the
871 somatosensory P300. J Neurosci 11:2039–2054.

872 Yeo BTT, Krienen FM, Sepulcre J, Sabuncu MR, Lashkari D, Hollinshead M, Roffman JL, Smoller
873 JW, Zöllei L, Polimeni JR, Fisch B, Liu H, Buckner RL (2011): The organization of the
874 human cerebral cortex estimated by intrinsic functional connectivity. J Neurophysiol
875 106:1125–1165.

876 Ziontz J, Adams JN, Harrison TM, Baker SL, Jagust WJ (2021): Hippocampal connectivity with
877 retrosplenial cortex drives neocortical tau accumulation and memory function. J Neurosci
878 41:8839–8847.

879

Supporting information

A role for retro-splenial cortex in the task-related P3 network

Diptyajit Das, Marnie E. Shaw, Matti S. Hämäläinen, Andrew R. Dykstra, Laura Doll, and Alexander Gutschalk

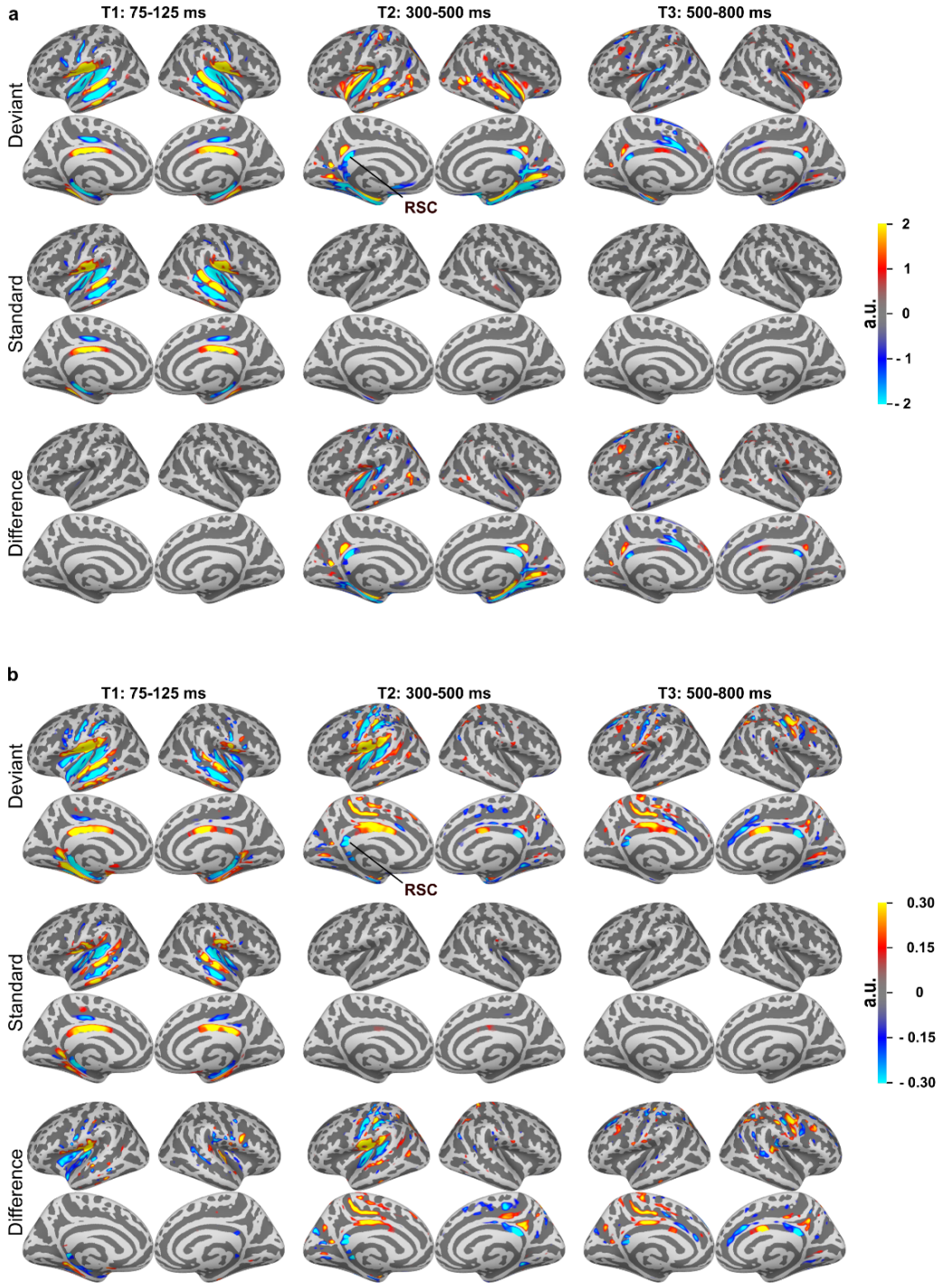

Figure S1 Cortical M/EEG and fMRI activation maps. These maps represent combined M/EEG source estimates similar to those shown in Figure 2a, but with alternative source analysis methods, using (a) sLORETA and (b) a Borgiotti-Kaplan beamformer. Note that the numerical values cannot be directly compared between these source estimation methods, even though they represent noise normalized z-scores.

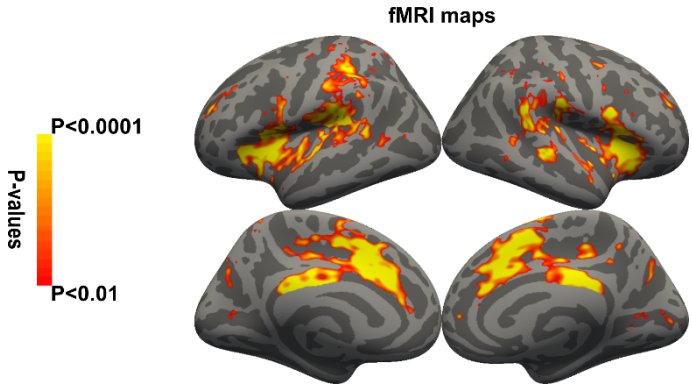

Figure S2 fMRI maps for the contrast deviants – standards, based on a random-effects statistic. Same analysis as Figure 2c but with more conservative cutoff (p<0.01, FDR corrected).

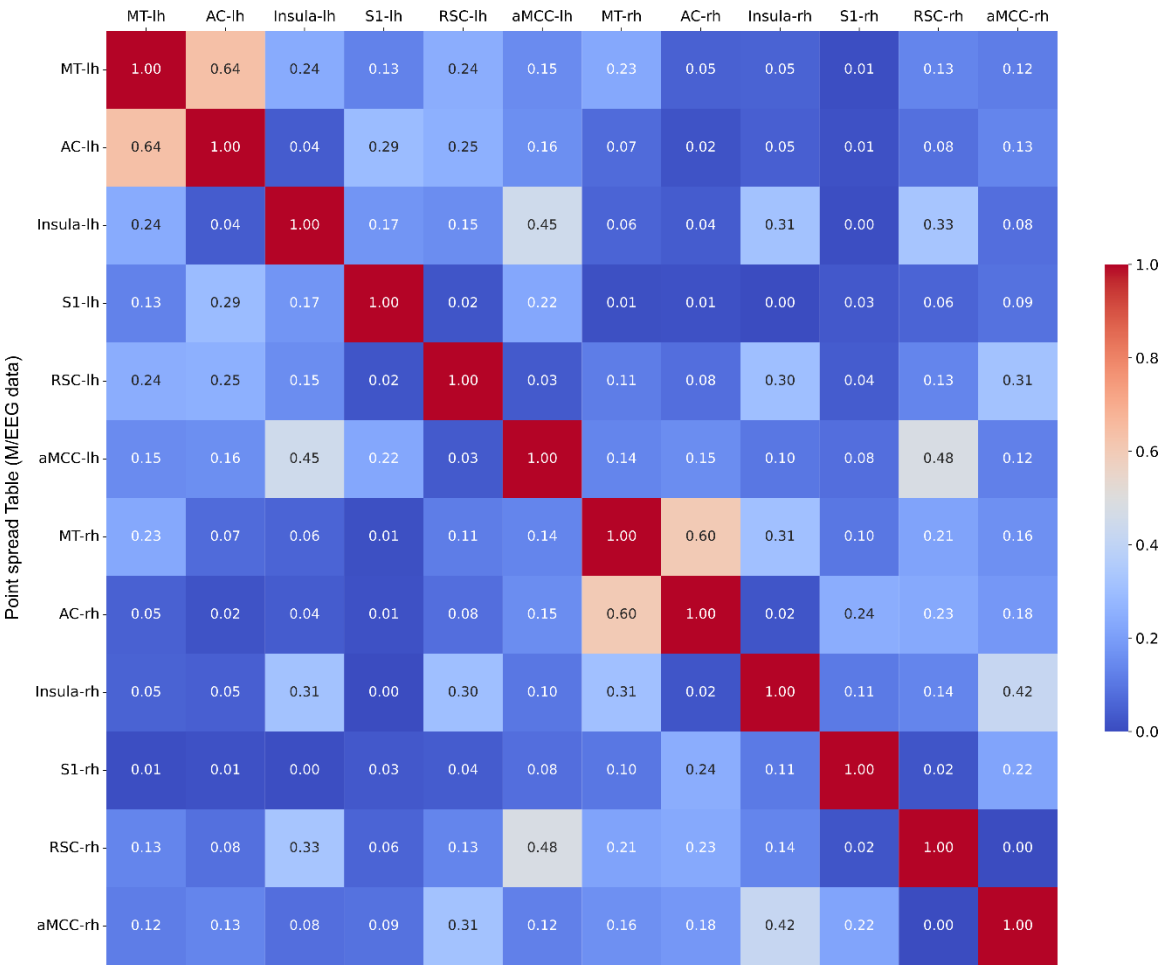

Figure S3 Point spread analysis table based on the M/EEG data. The spread values range from 0 (minimum) to 1 (maximum).

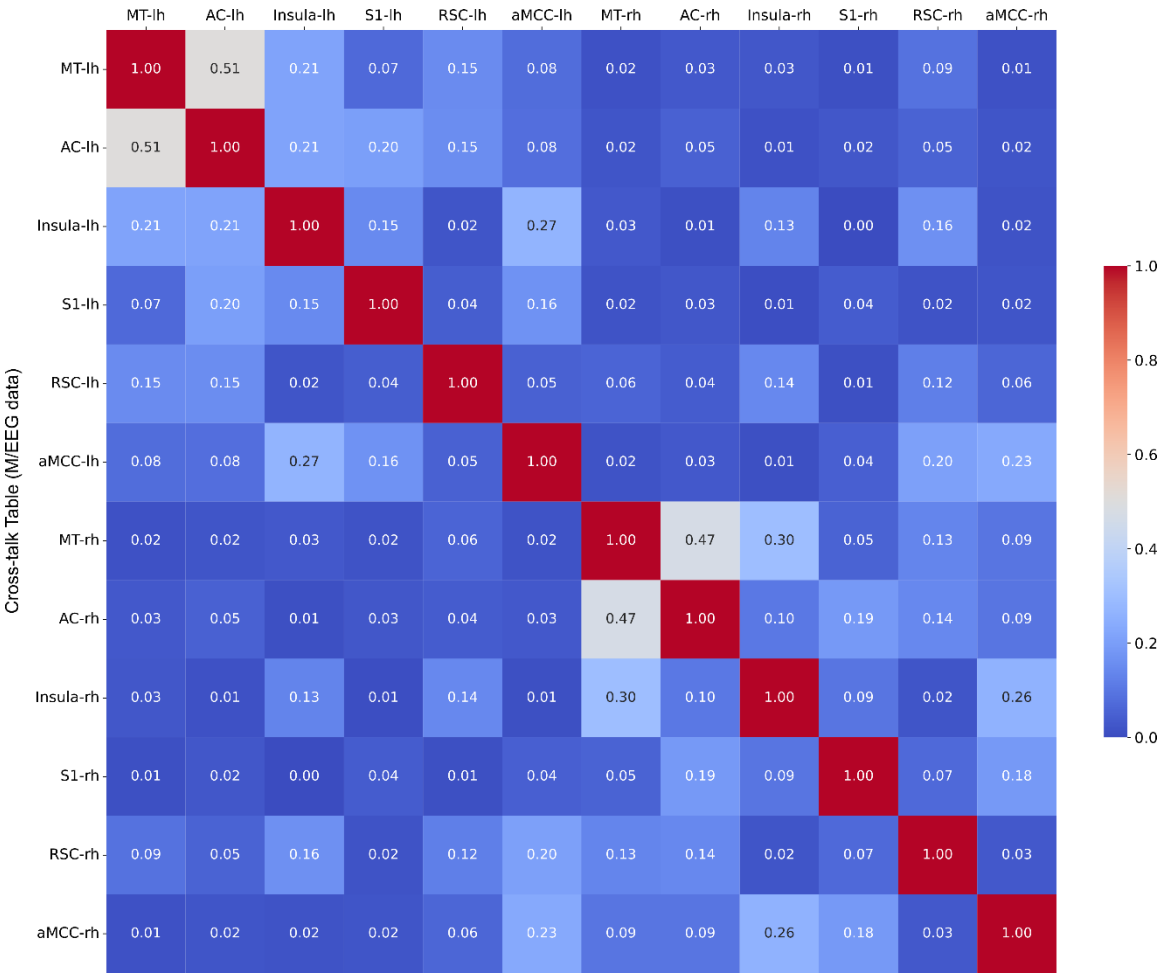

Figure S4 Cross-talk analysis table based on the M/EEG data. The cross-talk values range from 0 (minimum) to 1 (maximum).

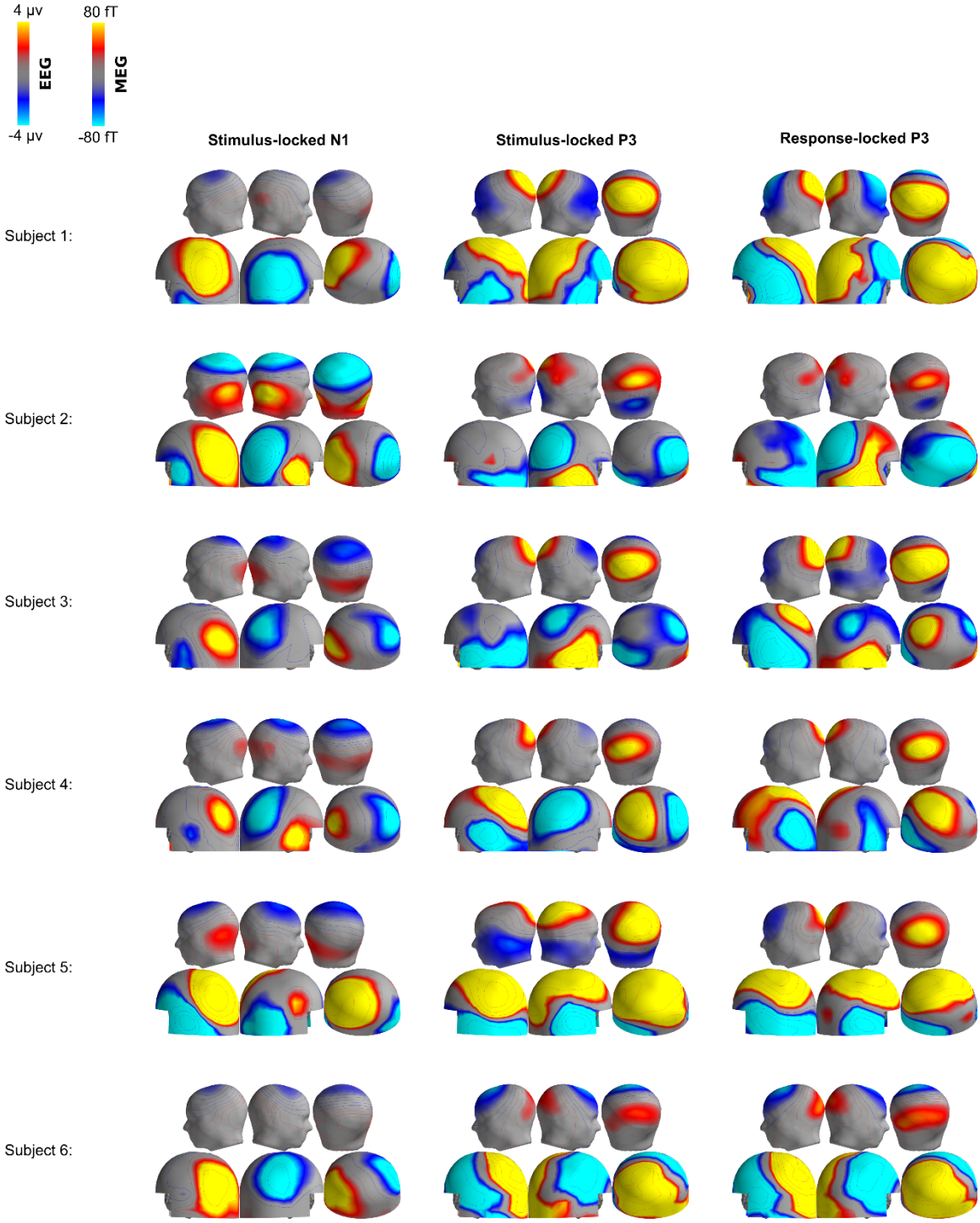

Figure S5 EEG and MEG maps for individual participants. The responses are mapped at the individual peak latency for N1 (left) stimulus-locked P3b (middle), and response-locked P3b (right) for individual participants 1 - 6.

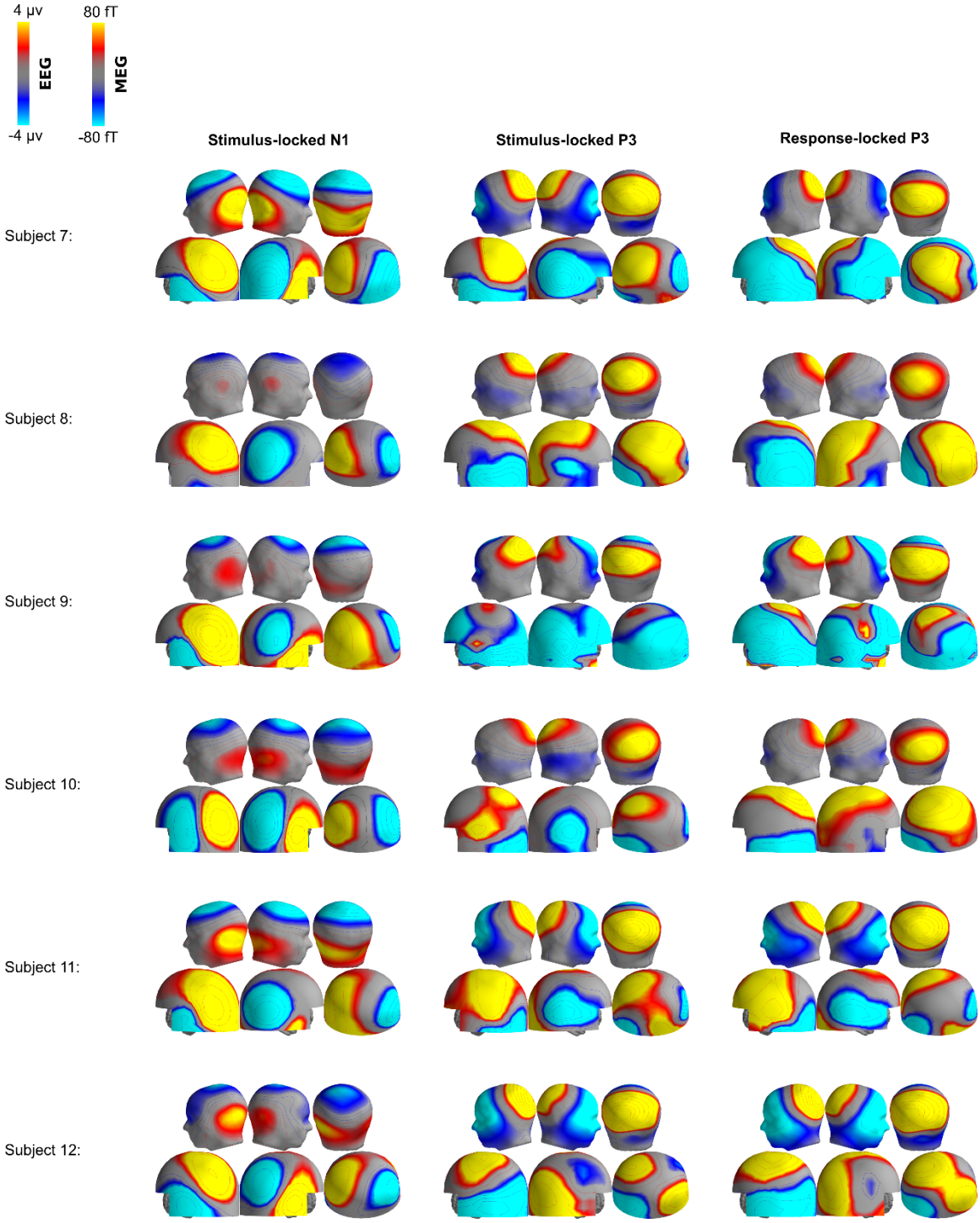

Figure S6 EEG and MEG maps for individual participants. The responses are mapped at the individual peak latency for N1 (left) stimulus-locked P3b (middle), and response-locked P3b (right) for individual participants 7 - 12.

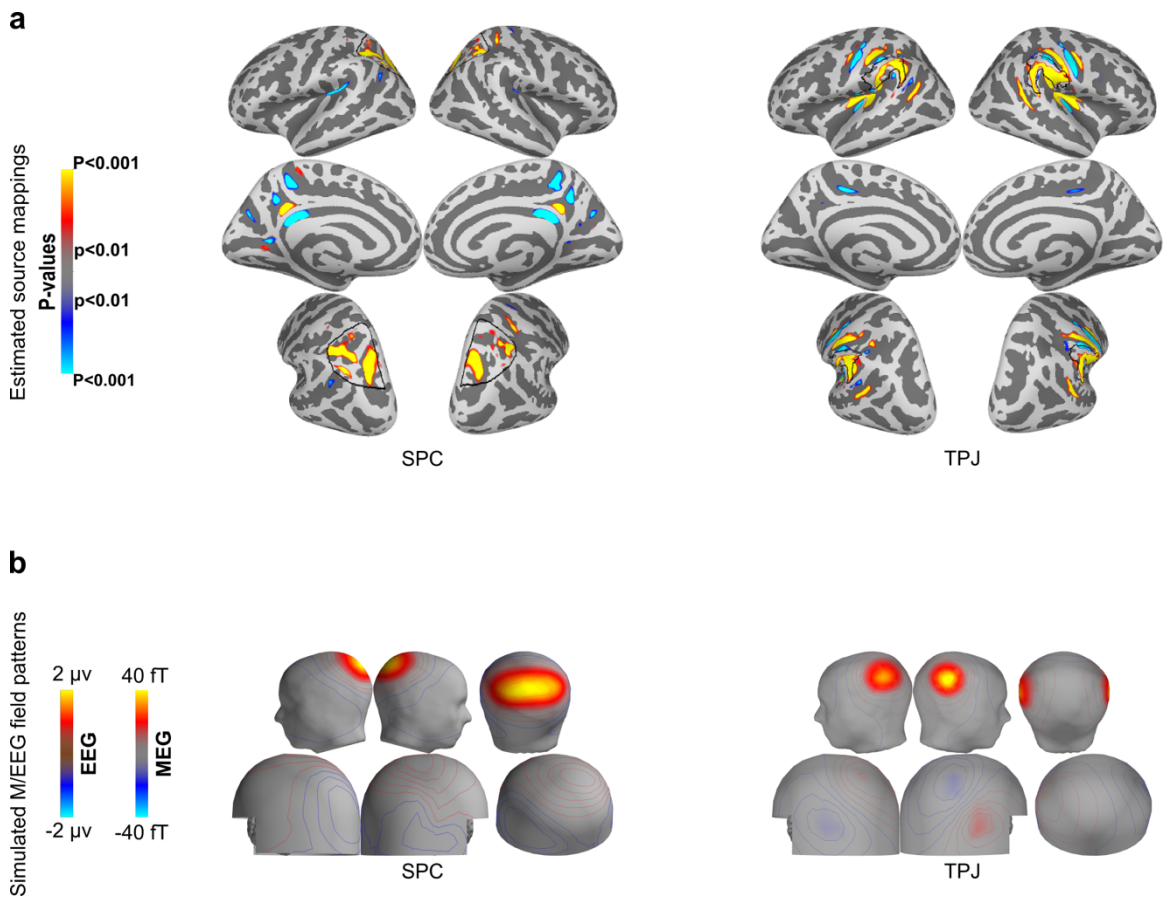

Figure S7 Simulated M/EEG for a distributed superior parietal cortex (SPC) and a temporo-parietal junction source (TPJ) source. (a) dSPM analysis for simulated distributed SPC (left) and TPJ (right) sources (n=12 subjects; p<0.01). (b) Average EEG and MEG maps for the simulated distributed SPC (left) and TPJ (right) sources.

Table S1 Modeling the grand-average N1 pattern with simulated M/EEG based on anatomically defined source regions (Figure 4b).

	Simulated source activation patterns					**Residual variance (RV) (%)**	
Source strength (nAm)	**AC**	**Insula**	**S1**	**RSC**	**aMCC**	**EEG**	**MEG**
	27.75	9.25	0.0	0.0	0.0	16.25	27.80
	28.75	-	-	-	-	20.70	26.80
	-	26.50	-	-	-	69.60	100.0

Table S2 Modeling the grand-average P3b pattern with simulated M/EEG based on anatomically defined source regions (Figure 4b). In this simulation, the extended superior parietal source (SPC; see Figure S6) is used instead of the retro-splenial cortex (RSC).

	Simulated source activation patterns					**Residual variance (RV) (%)**	
Source strength (nAm)	**AC**	**Insula**	**S1**	**SPC**	**aMCC**	**EEG**	**MEG**
	5.0	11.25	10.0	69.50	0.	8.90	66.60
	-	7.25	11.75	66.25	6.50	8.80	70.30
	3.0	-	11.25	64.0	6.25	8.0	73.40
	9.0	16.0	-	79.0	0.	11.10	75.10
	0.	0.	22.75	-	4.0	52.90	87.10
	5.0	11.25	10.0	69.50	-	8.90	66.60